4-2016

Nanoscale phonon thermal conductivity via molecular dynamics

Jonathan M. Dunn
Purdue University

PURDUE UNIVERSITY
GRADUATE SCHOOL
Thesis/Dissertation Acceptance

This is to certify that the thesis/dissertation prepared

By Jonathan Mark Dunn

Entitled
Nanoscale Phonon Thermal Conductivity via Molecular Dynamics

For the degree of   Master of Science in Materials Science Engineering

Is approved by the final examining committee:

Alejandro Strachan
_____
Chair

Eric Kvam

Ernesto Marinero

To the best of my knowledge and as understood by the student in the Thesis/Dissertation Agreement, Publication Delay, and Certification Disclaimer (Graduate School Form 32), this thesis/dissertation adheres to the provisions of Purdue University's "Policy of Integrity in Research" and the use of copyright material.

Approved by Major Professor(s):   Alejandro Strachan

Approved by: David Bahr   4/21/2016

Head of the Departmental Graduate Program   Date

NANOSCALE PHONON THERMAL CONDUCTIVITY VIA

MOLECULAR DYNAMICS

A Thesis

Submitted to the Faculty

of

Purdue University

by

Jonathan M. Dunn

In Partial Fulfillment of the

Requirements for the Degree

of

Master of Science in Materials Science Engineering

May 2016

Purdue University

West Lafayette, Indiana

ACKNOWLEDGEMENTS

The journey through graduate school has been one of the most challenging endeavors that I have ever chosen to undertake. It has stretched me in many ways, academically, emotionally, and spiritually, but through the faithfulness and help of my God, my family, my friends, and my coworkers, graduate school has been a period of great development in my life.

I would first like to thank my research advisor, Alejandro Strachan, for all of his time and advice in teaching me science and the research process. He has taught me many skills and disciplines needed to be an effective researcher.

I would also like to thank everyone in my research group and academic department who has supported me and contributed to my success, especially Edwin Antillon, whom I worked alongside more than anyone else, but also Nicolas Onofrio, David Guzman, Mitch Wood, Kiettipong Banlusan, Sam Reeve, Lorena Alzate, Hojin Kim, Yang Wang, Benjamin Haley, Anna Walters, John Rotella, and many others.

My thanks also goes to my loving wife, Bethany, whom I met and married while a graduate student and who has been my foremost supporter; my mentor, Ben Huckstep, who helped me to handle all of life's challenges that arose as a graduate student; and my family and friends who are always there to support me when I need it and who have never let me down.

TABLE OF CONTENTS

LIST OF TABLES

LIST OF FIGURES

ABSTRACT

Dunn, Jonathan M. MSMSE, Purdue University, May 2016. Nanoscale Phonon Thermal Conductivity via Molecular Dynamics. Major Professor: Alejandro Strachan.

Molecular dynamics (MD) simulations provide a useful and simple means of calculating the nanoscale thermal properties of materials, which requires special analysis since the thermal properties of materials change when their dimensions reach the nanoscale. In this research, MD is used to investigate the nanoscale phonon thermal transport of materials that are attracting much interest in the areas of materials science and nuclear physics. In order to evaluate two distinct methods of calculating the thermal conductivity of materials using MD, the simulation methods are first applied to Si. Once an understanding of each simulation method is established, they are then used to analyze the thermal conductivity of $MoTe_2$ and $MoTe_2Cu$, which are lesser-researched two-dimensional materials with promising applications in nanotechnology. Lastly, the simulations methods are applied to calculate the thermal conductivity of nuclear matter, which is formed within the extreme conditions of neutron stars. The high temperatures of neutron stars cause protons and neutrons to break apart from their usual nucleic form and instead bond together to form much larger structures. Research into these materials will advance the development of nanotechnology as well as contribute to the ongoing research to better understanding the thermal processes that occur within neutron stars.

The two methods of thermal conductivity simulations used in this research are the thermostat method and the Müller-Plathe method. The thermostat method is analyzed using two thermostats: the Nosé-Hoover thermostat and the Langevin thermostat. When evaluating these simulation methods using Si, it is found that the Müller-Plathe method and the Nosé-Hoover thermostat method give very similar results that align with published values, whereas the Langevin results differ considerably, giving larger values than the other methods. The reason of this difference is that the Langevin thermostat affects the phonons of

the system, which changes the phonon transport properties of the system and causes an increase in the thermal conductivity. This result demonstrates that the means of energy input into a system can affect its thermal transport properties, which provides an additional means of controlling nanoscale thermal transport properties for nanotechnology applications.

Because no values for the thermal conductivity of $MoTe_2$ have yet been published, this research provides an initial description of it thermal transport properties. Using a recently developed reactive force field, the thermal conductivity of $MoTe_2$ is calculated to range from 1-3 W/mK for channel lengths of 10-150 nm, which fits well with the thermal properties of other materials in the same class. Intercalating Cu into the $MoTe_2$ modifies slightly its thermal properties and can be used as a means of engineering a precise thermal conductivity value for nanoscale devices.

The investigation into nuclear matter is to contribute to research endeavors into the thermal properties of neutron stars. Because of the high temperature of neutron stars, temperature is measured in MeV rather than K. Instead of analyzing size-effects on thermal conductivity, the goal is to measure the changes in thermal conductivity as the nuclear matter undergoes phase-transitions at various temperatures. The results indicate that the thermal conductivity of nuclear matter decreases from around 5 W/mMeV to 2.5 W/mMeV as the temperature is increased from 0.48-0.86 MeV, with phase transition occurring at around 0.6 MeV and 0.8 MeV.

CHAPTER 1: INTRODUCTION

Nanotechnology is a rapidly developing area of research in today's scientific community. Two of the primary approaches to improving current nanotechnology applications are to take existing technological designs and fabricate them on a smaller scale, or to develop new materials with improved material properties that provide better performance than the current choice of materials. One of the numerous aspects of device design that must be taken into consideration in nanoscale device design is the thermal properties of the system. The importance of thermal management in nanotechnology is easily pictured when considering the purpose of nanotechnology: to perform more work on a smaller scale. Because work generates heat, the larger work density present in, for example, nanoscale circuits means greater amount of self-heating, and as material properties are often temperature dependent, increasing temperatures will diminish the performance of nanotech devices.[1,2] One of the most straightforward approaches to managing thermal problems is to enhance the thermal conductivity of the materials present in the device so that heat can be dissipated more easily.[3] A deeper understanding of the thermal transport of materials is therefore of great use in advancing nanotechnology.

Current scientific literature demonstrates many of the applications for which controlling the thermal transport of materials is of great benefit in device performance. The problem of self-heating is prominent in electronic chips with high power-densities,[1] which decreases the performance of the electronic circuits[4] and can shorten the lifespan of the device.[2] Self-heating is also a problem in silicon-on-insulator transistors[5] as well as data-storage devices in which heating problems can cause loss of stored data.[6] Other applications, such as lasers, require effective heat removal to maintain the high power levels needed for optimal performance.[7] Advancements in nanostructuring create new thermal transport challenges as the complex structures of nanostructured materials can make heat removal more difficult.[1] An understanding of thermal transport mechanisms will aid in each of these

technological developments as it would provide insight into efficient means of heat removal, which would improve device performance.

1.1 Thermoelectric Devices

One of the most promising applications involving the advancement of nanoscale thermal control is the development of thermoelectric materials. When a temperature gradient is imposed on a thermoelectric material, the electrons in the hot region occupy higher energy states than the electrons in the cold end and begin to diffuse from the hot to the cold region.[8] This phenomenon gives thermoelectric materials the unique ability of producing an electric current by means of a temperature difference, and vice versa.[9] In this way, heat can be used to produce electric power, or, inversely, electric power can be used to produce a temperature gradient, which can function as a type of refrigerator.[10] Thermoelectrics are a well-established area of research, but their efficiency of energy conversion has not yet reached high enough levels for commercial applications.[11] A measure of thermoelectric efficiency is characterized by the "figure of merit" value of ZT:

$$ZT = \frac{S^2 \sigma T}{\kappa} \qquad (1.1)$$

where S is the Seebeck coefficient—a measure of induced thermoelectric voltage—, σ is the electrical conductivity, T is the temperature, and κ is the thermal conductivity. A higher ZT value corresponds to a higher energy conversion efficiency. In order to improve the efficiency of thermoelectric materials, the thermal conductivity needs to be minimized and the electrical conductivity needs to be maximized.[12]

A difficulty in improving the thermoelectric efficiency arises in many materials because the electrons in the material contribute to both electrical and thermal conductivity. Consequently, increasing or decreasing one value will usually move the other value in the same direction, which does little to improve efficiency. One approach to overcome this positive correlation is to employ semiconductors in thermoelectric designs because the electrical and thermal conductivities are less coupled in semiconductors due to the presence of fewer conduction band electrons. In semiconductors such as Si, the thermal conductivity

is dominated by phonons, as will be discussed in section 1.3.1. Therefore, by manipulating the phonons of a semiconductor, the thermal conductivity can be reduced while having a minimal effect on the electrical conductivity.[10] One of the most promising means of reducing the thermal conductivity of bulk materials is via nanostructuring. Si nanowires, for example, have the same Seebeck coefficient and electrical conductivity of bulk Si but possess a 100-fold lower thermal conductivity.[13] The small dimensions of nanowires increase phonon scattering and thereby reduce the thermal conductivity.[8] Before means of producing nanowires had been developed, *ZT* values had never exceeded 1, but current research into nanomaterials has produced nanostructured semiconductors that reach *ZT* values of 2.5.[14] Once a *ZT* value of 3 has been reached, it is estimated that thermoelectric devices will be able to produce electrical power as efficiently as modern gas-powered devices.[7] Achieving this remaining increase in efficiency calls for further analysis into how lowering the dimensions of a material to the nanoscale affects the thermal properties of the material.

1.2 Thermal Transport at the Nanoscale

In order for thermal transport to occur within a material, there must be an energy carrier that transports energy within the material from one region to another. The two types of energy carriers within materials are electrons and phonons. In metals, free-flowing electrons contribute significantly to thermal conduction, but in semiconductors, only the few number of conduction band electrons are able to move through the material, dramatically decreasing the contribution of electrons to thermal transport. Phonons are, therefore, the primary means of thermal transport in semiconductors, making such materials prime candidates to study how manipulating phonons can lead to means of controlling the phonon thermal conductivity of materials. An analysis of phonon thermal conductivity, however, should begin by laying down the foundational concepts of phonons to build the framework for understanding means of thermal control in materials.

1.2.1 Thermal Transport via Phonons

   A conceptual description of phonons begins with the atomic structure of materials. Atoms in a crystalline solid are arranged in a periodic, organized manner that can be described by a specific set of basis vectors. These mathematically precise basis vectors define the equilibrium position of every atom in the crystal, but the kinetic energy of each atom means that every atom is constantly vibrating around its equilibrium position. However, the interaction of an atom with its neighboring atoms due to interatomic forces means that the vibration of each atom is influenced by the vibrations of its neighbors. Consequently, atomic vibrations are correlated and form vibrational waves that travel through the crystalline lattice with a specific frequency, wavelength, and amplitude. These waves are known as lattice vibrations, and the quantum—the smallest, discrete element—of a lattice vibration is known as a phonon.[15] In concise terms, phonons are vibrational waves that travel though a material via coherent atomic vibrations. Using this conceptual definition of phonons, thermal transport via phonons can be easily pictured. As atoms vibrate in a coherent manner, they transfer kinetic energy to one another. A series of atomic vibrations that passes through a material in wave-like manner means that the atoms are passing kinetic energy one to another along the path of the vibration. In this way, a phonon transports kinetic energy across a material.

   Phonons have several properties that are crucial in controlling the thermal conductivity of a material. First of all, phonons are able to interact and mutually alter the direction they are travelling. The average distance phonons travel within a material without a scattering event causing them to change directions is known as the phonon mean-free-path (mfp). When phonons are scattered often, they are unable to transport energy across a material very quickly. As a result, the thermal conductivity of the material will be low. Phonons with a large mfp will traverse a much larger distance before scattering, and the thermal conductivity will be greater. A simple approximation for phonon thermal conductivity is given by the equation

$$\kappa = \frac{1}{3} C_v v l \tag{1.2}$$

where C_v is the volumetric specific heat, v is the phonon group velocity, and l is the phonon mfp.[16] The main inaccuracy of this equation lies in its assumption that the energy and

velocity of all phonons are equal, which is not the case for real systems. For real systems, the volumetric specific heat, phonon group velocity, and scattering rate are frequency dependent, and the equation becomes

$$\kappa = \frac{1}{3} \sum \int C_v(\omega) v(\omega) l(\omega) d\omega \qquad (1.3)$$

where ω is the phonon frequency.[17] The phonon mfp of the system is also affected by the temperature of the system. At low temperatures, typically $T < 50$ K, the low kinetic energy of the atoms results in low-intensity vibrations, which makes phonons less likely to interact and scatter. Without the interaction and scattering of phonons, there is an upward trend in the phonon mfp of materials from 0 K to around 50 K. At 50 K, this increasing trend reverses due to high-energy phonons beginning to scatter one another. By the time materials reach room temperature, the frequent scattering of high-energy phonons results in thermal transport occurring primarily through low-energy, long-wavelength phonons because of their higher mfp.[8] For room-temperature semiconductors, the phonon mfp ranges from 10-100 nm[18] with wavelengths of 3-10 nm.[19]

1.2.2 Nanoscale Effects on Thermal Transport

Of key interest to current research into controlling the thermal properties of materials is the effect of nanoscale dimensions on phonon thermal conductivity. Whereas many material properties are independent of size for macroscale materials, this is not always the case for nanoscale materials. At the nanoscale, the dimensions of a material become comparable in size to its phonon mfp.[18] This dramatic increase in surface area to volume ratio means that a much larger percentage of phonons will be scattered by the surface of the material,[17] effectively lowering the phonon mfp and thermal conductivity.[12] Surface scattering on semiconductor thin films with thickness on the order of 100-1,000 nm results in a 10-50% decrease in thermal conductivity from bulk values,[4] and nanowires have been demonstrated to possess thermal conductivity values up to a factor of ten lower than bulk values.[8] Of additional benefit is that nanoscale dimensions, while having a large effect on thermal conductivity, have a minimal effect on electrical conductivity since the mfp of electrons is still much lower than the dimensions of the material.[10] By taking advantage of

the size dependence of thermal conductivity for nanoscale materials, the thermal conductivity of bulk structures can be controlled via nanostructuring. Producing bulk materials by constructing an extensive array of nanoscale structures will yield macroscale objects that will retain the thermal properties of the constituent nanoscale structures. The current work in this area of research is to develop a deeper understanding of the nanoscale properties of materials. Whereas nanoscale materials are harder to examine in a laboratory due to the small scale of the material and the difficultly in quickly and easily producing materials on that scale, atomistic simulations are well-suited to examine the properties of such materials as they are able to simulate the number of atoms present in a nanoscale material. In particular, molecular dynamics (MD) simulations are ideal for this work as they inherently capture the vibrations of atoms that give rise to phonons.

1.3 Molecular Dynamics

The two main approaches to atomistic simulations are density-functional theory (DFT) and molecular dynamics (MD). Whereas DFT is based upon quantum theory and is able to perform *ab-initio* calculations using the inherent electronic properties of atoms, MD uses classical mechanics to describe the time-evolution of a system of particles. To compensate for the classical approximations, MD requires a material-specific input of interatomic potentials, which are often developed using DFT calculations. MD is advantageous over DFT to study phonon thermal transport for several reasons. First, the classical description of particles inherently captures the atomic vibrations that give rise to phonons, and the electronic picture included in DFT is not needed since electronic thermal transport is negligible in semiconductors. Secondly, quantum calculations makes DFT computationally expensive and limits it to smaller systems of no more than several hundred atoms. MD can simulate larger systems of hundreds of thousands of atoms, which is needed to capture the scale at which phonons travel.

The foundation of MD simulations are the classical equations of motion

$$\dot{r}_i = v_i \qquad (1.4)$$

and

$$\dot{v}_i = \frac{F_i}{m_i} \qquad (1.5)$$

which are integrated at periodical intervals of time to model the time-evolution of a system of particles. To begin a simulation, a velocity is generated for each atom according to a set distribution, which establishes the initial temperature of the system. The interatomic potential is then used to adjust the velocity of each atom according to the forces it experiences from its neighboring atoms. The simulation will then advance one timestep by repositioning each atom according to where it would be if it moved along its velocity vector for the span of one timestep. Then a new velocity is calculated for each atom according to the interatomic forces it now experiences, and the simulation advances another timestep. The repetition of this cycle generates the time-evolution of the system. The timesteps for MD simulations are usually on the femtosecond timescale range as that is order on which the fastest atomic vibrations occur within a solid.

The interatomic potentials required in MD simulations describe the potential energy of atoms as a function of position, which provides a simple means of calculating interatomic forces as force is the negative gradient of the potential energy. Interatomic potentials are often developed through DFT simulations that use the electronic properties of atoms to calculate the potential between them. An alternate approach to using calculated parameters that describe the interatomic potentials is to input tabulated experimental data of potential energy versus separation distance between two particles.

1.4 Thesis Outline

Having provided a foundational understanding of nanoscale phonon thermal transport and MD simulations, chapter 2 of this thesis will outline the simulation methods used to calculate the thermal conductivity of materials. The two simulations methods are the thermostat method and the Müller-Plathe method. Chapter 3 will then provide an analysis of these simulation methods by comparing their performances in calculating the thermal conductivity of Si, which is a well-researched material and provides a sort of standard for these simulation methods. Chapter 4 covers the application of the Müller-Plathe simulation

method to calculate the thermal conductivities of $MoTe_2$ and $MoTe_2Cu$, materials which are gaining interest in the scientific community and for which no thermal conductivity values have yet been published. Chapter 5 advances the ability of MD to simulate unique materials in extreme environments by calculating the thermal conductivity of the nuclear matter found in neutron stars. Nuclear matter is made up of protons and neutrons at high enough temperature that they are no longer bound together in a nucleus and instead form much larger structures. Lastly, chapter 6 concludes the results presented in this thesis and provides an outlook for potential future research endeavors to delve further into understanding these nanoscale thermal transport phenomena.

CHAPTER 2: SIMULATION DESIGN

Several methods have been developed to calculate thermal conductivity using MD simulations. Each calculation method can be classified as either an equilibrium MD (EMD) method or a nonequilibrium MD (NEMD) method. The most popular EMD method is the Green-Kubo approach, which uses the fluctuation-dissipation theorem to calculate transport coefficients according to the formula

$$\kappa = \frac{V}{3k_B T^2} \int_0^t < J(t)J(0) > dt \qquad (2.1)$$

where V is the volume of the system, k_B Boltzmann's constant, T is temperature, and J is the heat current tensor. In this manner, the Green-Kubo approach calculates thermal conductivity by time-averaging the instantaneous fluctuations in heat flow in a system at equilibrium. Conversely, NEMD simulations use a steady-state heat flow to calculate the thermal conductivity.[16] The general approach to NEMD thermal conductivity simulations is to establish a constant heat flow along the simulation structure and then allow the corresponding temperature gradient to form. The heat flow and temperature gradient of the system can be used to calculate the thermal conductivity of the material through a simple application of Fourier's Law.

2.1 Fourier's Law

NEMD simulations calculate the thermal conductivity of a material by establishing a heat flow and temperature gradient within a material and examining the relationship between them. Fourier's law states that thermal conductivity is the negative ratio of heat flux to temperature gradient, or

$$\kappa = -\frac{J}{\nabla T} \qquad\qquad (2.2)$$

where J is the heat flux and ∇T is the temperature gradient. Heat flux—the rate of heat flow through the cross-sectional area of the material—is used instead of the rate of heat flow to normalize the amount of heat flow according to the amount of material contributing to the heat flow. The negative in the equation is to dictate that heat flows from an area of higher temperature to an area of lower temperature.[16]

Much debate has occurred over whether Fourier's law is valid for nanoscale materials.[20,21] Fourier's law is clearly demonstrated for macroscale materials, but has an undeveloped theoretical basis that has caused its applicability to nanoscale materials to be, until recently, uncertain.[20] Recent research, however, has demonstrated the validity Fourier's law at the nanoscale by showing that Fourier's law and the phonon Boltzmann transport equation produce the same results, given that jumps in the temperature of the system near the hot and cold reservoirs are taken into account when calculating the temperature gradient.[22] These temperature jumps near hot and cold reservoirs in a nanoscale system are real features of nanoscale heat transport that can be easily reproduced in MD simulations. The resulting temperature gradient will not be equivalent to the temperature difference between the reservoirs divided by the distance between them. The appropriate temperature gradient is calculated by considering only the linear region of the temperature profile and ignoring the temperature jumps. For further insight into these temperature jumps, see Ref. 22.

2.2 The Thermostat Method

The first NEMD simulation method used for this research, called the thermostat method, calculates thermal conductivity by creating a temperature difference between a hot region and a cold region and observing the resultant heat flow and temperature gradient. To begin, the simulation structure is divided into two contacts, a hot and a cold, with two channels placed in between the contacts (Fig. 2.1). The structure is set to be periodic in the heat flow direction, which allows phonons to travel in the thermal transport direction without being disrupted when reaching the end of the simulation structure. In this way, the scattering

of phonons at surfaces depends only on the boundary conditions in the lateral dimensions, which more appropriately resembles thermal transport along a nanowire or across a thin film. If the lateral dimension are set with periodic boundary conditions, then the structure represents a lattice of thin films separated by hot and cold contacts. But if the lateral dimensions are set to non-periodic boundary conditions, then the structure becomes an infinite sequence of nanowires set end-to-end to one another. In this way, with only a simple switch of the boundary conditions, the thermal conductivity of both thin films and nanowires can be analyzed.
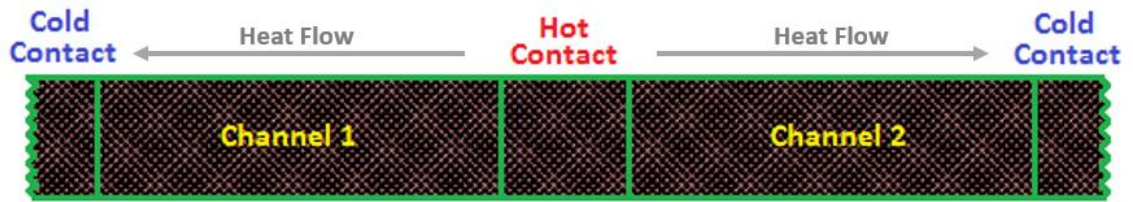
Figure 2.1: Specimen structure for the NEMD thermostat method of calculating thermal conductivity. The structure is divided into a hot bin and a cold bin with a two channels place in between them. The periodic boundary conditions in the heat flow direction joins together the two cold half-contacts. The simulation structure causes heat to flow in opposite directions along the channels from the hot to cold contact.

The temperature difference between the hot and cold bin is established at the start of the MD simulation by setting the contacts to their respective temperatures. Once the simulation begins, heat will begin to flow from the hot contact to the cold contact, driving the system towards thermal equilibrium. To keep the contacts at their respective hot and cold temperatures, the thermostat method applies a thermostat to each contact. Thermostats are temperature control algorithms that can be applied to a group of atoms to ensure that they maintain a constant temperature. For this study, the Nose-Hoover and the Langevin thermostats were used to examine their effectiveness in simulating thermal transport in materials. The work of the thermostats is to add or remove energy from the hot and cold contacts to maintain their respective temperatures as heat transport continues. In this manner, the MD simulation creates an indefinite flow of heat through a material that can be analyzed to calculate the thermal conductivity. It is crucial that the system reaches steady-state heat transport before calculating thermal conductivity to ensure that the temperature gradient and

rate of heat flow are not changing over time except for the natural fluctuations found in dynamical systems.

Once the system has reached steady-state heat flow, the thermal conductivity can be determined by calculating the temperature gradient and heat flux and then applying Fourier's law. When in steady-state, the energy added into each contact by the thermostat to maintain its temperature will be equivalent to the energy leaving or entering the contact due to the heat flow. Conveniently, the cumulative energy added by a thermostat into a contact can be obtained as a thermodynamic output of the MD simulation, and its time derivative is the corresponding heat flow of the system (Fig. 2.2a). However, because heat is flowing out of the hot contact in opposite directions along the two channels, the actual amount of heat traveling along either one of the channels is one-half of the total amount of heat leaving the hot contact, and so the time derivative of the cumulative energy inputted by the contacts must be dividing by two to obtain the rate of heat flow. Next, to calculate the temperature gradients of the channels, the simulation structure is divided at the start of the simulation into a series of bins in the heat transport direction. At each timestep, the kinetic energy of the particles in each bin is calculated and averaged to provide the instantaneous temperature of every bin. This collective series of bin temperatures, when plotted against position, provides the instantaneous temperature profile of the simulation structure. Once the system reaches steady-state, then the temperature of each bin at every timestep is averaged together to create a time-averaged temperature profile that averages out any temperature fluctuations that may appear in any instantaneous snapshot (Fig. 2.2b). Using this temperature profile, a linear fit of the bins within the channel yields the temperature gradient of the system. Then, after converting the heat flow rate to heat flux, the thermal conductivity can easily be calculated by dividing the heat flux by the temperature gradient.
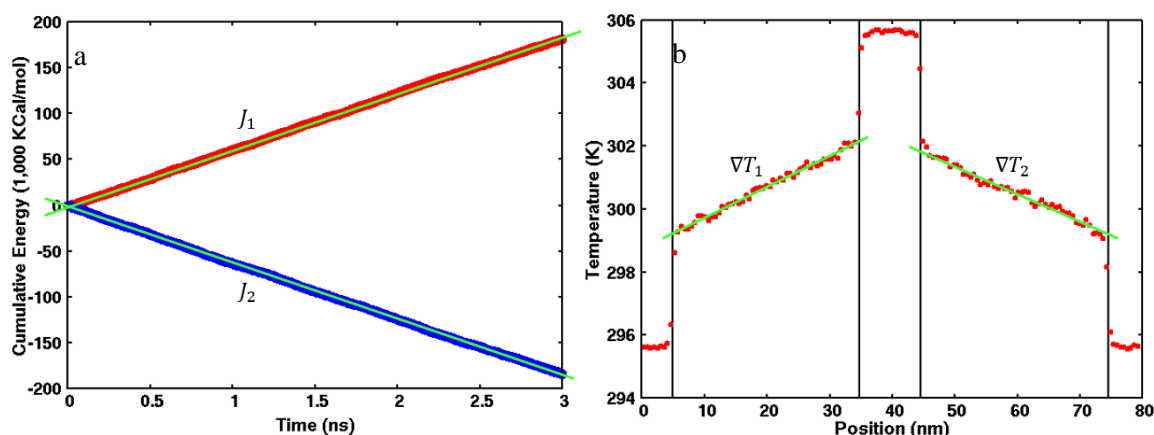
Figure 2.2: (a) The cumulative energies added by the thermostats into the hot (red) and cold (blue) contacts. A linear fit yields the twice the rate of heat flow through the channels since heat flows out of the hot contact in opposite directions. (b) A temperature profile from a NEMD thermal conductivity simulation using the thermostat approach. From this profile, the temperature gradient can be calculated by fitting a line to the linear region of the profile. The temperature jumps near the contacts can also be seen.

2.3 The Thermostats

Several thermostats have been developed to provide temperature control mechanisms in MD simulations. The general premise behind thermostat algorithms is to modify the normal MD equations of motion to include a term that controls the energy of the thermostatted atoms. A common thermostat method is to place the thermostatted atoms next to an infinite, fictitious heat bath that is set to the target temperature. The idea is that heat will flow between the heat bath and the thermostatted atoms to keep the thermostatted atoms at the temperature of the heat bath. Since the heat bath is infinite, its temperature will remain constant at the target temperature despite the interchange of energy with the thermostatted atoms. For this study, the two thermostats used are the Nosé-Hoover thermostat and the Langevin thermostat. The algorithms for these two thermostats will be examined to provide an analysis of their temperature control mechanisms.

2.3.1 The Nosé-Hoover Thermostat

As previously explained in section 1.4, the normal MD equations of motion are given by

$$\dot{r_i} = v_i \tag{2.3}$$

and

$$\dot{v_i} = \frac{F_i}{m_i} \tag{2.4}$$

The Nosé-Hoover thermostat adds to these equations a dynamical variable known as the heat flow variable (ξ):

$$\dot{v_i} = \frac{F_i}{m_i} - \xi v_i \tag{2.5}$$

ξ is defined by its derivative as

$$\frac{d\xi}{dt} = \frac{1}{Q} \sum_{i=1}^{N} m_i |v_i|^2 - 3Nk_B T_0 \tag{2.6}$$

where Q is the mass of fictitious particles from which energy is being pulled in the system to maintain constant temperature, N is the number of thermostatted atoms, k_B is Boltzmann's constant, and T_0 is the temperature the thermostat is set to maintain.[24,25] It is often more convenient use the relaxation time (τ) of the thermostat in place of Q via the equation

$$\tau^2 = \frac{Q}{3Nk_B T_0} \tag{2.7}$$

which yields

$$\frac{d\xi}{dt} = \frac{1}{\tau^2} \frac{\sum_{i=1}^{N} m_i |v_i|^2}{3Nk_B T_0} - 1 \tag{2.8}$$

This formula can be transformed into the simple equation[26,27]

$$\frac{d\xi}{dt} = \frac{1}{\tau} \left(\frac{T_0}{T(t)} - 1 \right) \tag{2.9}$$

An examination of this equation reveals how the Nosé-Hoover thermostat uses an integral feedback mechanism to add or remove the appropriate amount of energy from the system to reach the target temperature. By comparing the target temperature (T_0) to the current temperature ($T(t)$), the thermostat algorithm calculates the necessary magnitude of the heat flow variable to adjust the energy of the thermostatted region to the target temperature.

However, because the Nosé-Hoover thermostat considers the temperature of the thermostatted region as a whole and then applies the same magnitude of correction to all atoms, it does nothing to ensure that every atom resides at the target temperature. In other words, temperature gradients are allowed to form within the thermostatted region as long as its average temperature equals the target temperature. Another aspect of the Nosé-Hoover thermostat that holds particular significance to thermal conductivity calculations is the role of the relaxation time (τ). The relaxation time determines how often the Nosé-Hoover thermostat checks the temperature of the thermostatted region and adjusts it accordingly. A smaller value of τ means that the Nosé-Hoover thermostat adjusts the temperature more frequently, resulting in a strong coupling between the actual temperature and the target temperature. A higher value of τ means that the atoms are allowed to relax for a longer time before their energies are adjusted, which means they are less strongly coupled to the target temperature. In this sense, thermostats can be referred to as "strong" and "weak" based upon their τ value. If τ becomes large enough, heat will begin to flow out of the thermostatted region faster than the thermostat can make the necessary temperature adjustments, in which case the thermostat is said to be failing. The role of the relaxation time on thermal conductivity results will be discussed in section 3.3.1.

2.3.2 The Langevin Thermostat:

The Langevin thermostat, instead of using a feedback mechanism like the Nosé-Hoover thermostat, adds two additional force terms to the MD equations of motion to control atomic temperatures:

$$\dot{v}_i = \frac{F_i}{m_i} - \frac{v_i}{\tau} - \frac{R}{m_i}\sqrt{\frac{m_i k_B T_0}{\tau \Delta t}} \qquad (2.10)$$

where the second term—velocity divided by the relaxation time—acts as a frictional force on the thermostatted particle, and the third term is a stochastic force modeling fictitious solvent particles at the target temperature (T_0) which "collide" with the thermostatted particles to keep them at constant temperature. τ is, again, the thermostat relaxation time, Δt is the time step of the simulation, and R is a uniformly distributed random variable between -1 and 1 that determines the direction and magnitude of the fictitious collisions.[26,27] Because the

equations treat the particles as if they are solvated within a fictitious system kept at T_0, the particles are effectively kept at T_0. The relaxation time (τ), as in the Nosé-Hoover thermostat, determines the strength of the thermostat as it defines the frequency of the fictitious collisions. But unlike the Nosé-Hoover thermostat, which adjusts energy input into the system as a whole, the Langevin thermostat acts on every atom in a way that keeps all of them at the target temperature, eliminating the possibility of temperature gradients forming within the thermostatted region.

2.4 The Müller-Plathe Method

The other NEMD thermal conductivity simulation method used in this research is called the Müller-Plathe method after its originator. Whereas the thermostat approach uses thermostats to create a temperature difference that drives heat flow, the Müller-Plathe method initiates heat flow and then allows a temperature gradient to form to match it. The Müller-Plathe method begins by dividing the simulation structure into an even number of bins in the heat flow direction (Fig. 2.3). The first bin is dubbed the cold bin and the n/2 + 1 bin is dubbed the hot bin. Then, to generate heat flow, the most energetic particle in the cold bin is swapped at periodic time intervals with the least energetic particle in the hot bin.[16,28,29] This swapping causes the hot bin to rise in temperature, which spurs heat flow towards the cold bin. As the swapping continues, the temperature of the hot bin will increase until the rate of heat flow matches the rate at which energy is being transferred from the cold to hot bin via swapping, at which point the simulation has reached steady-state. Because the temperatures of the hot and cold bin are not set, the steady-state temperatures of the hot and cold bins will depend on the swap rate, with a higher swap rate resulting in a larger temperature difference between the bins.
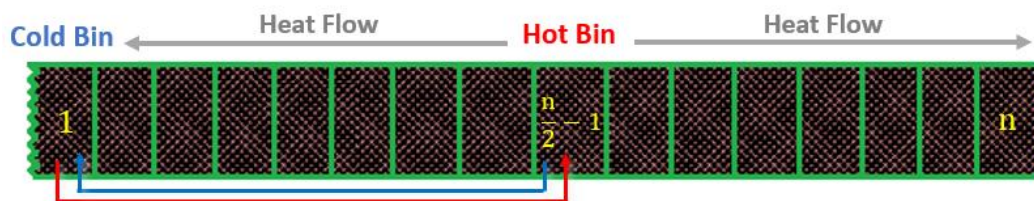
Figure 2.3: Simulation design for the Müller-Plathe method of calculating thermal conductivity. The simulation structure is divided into n number of bins in the heat flow direction, with bin 1 being the cold bin and bin n/2 − 1 being the hot bin. At a periodic number of timesteps, the hottest particle in the cold bin is swapped with the coldest particle in the hot bin, resulting in heat flow from the hot bin in both directions towards the cold bin.

The thermal conductivity calculation using the Müller-Plathe method follows the same approach as used in the thermostat method. The time-averaged temperature is calculated for a series of bins in the heat transport direction to produce a temperature profile of the system (Fig. 2.4a). The linear portion of the temperature curve is used to measure the temperature gradient. The rate of heat flow is calculated by taking the time derivative of the cumulative energy swapped between the cold and hot bins (Fig. 2.4b). This value for cumulative energy is obtained as a thermodynamic output from the simulation. The thermal conductivity is then calculated using Fourier's law.
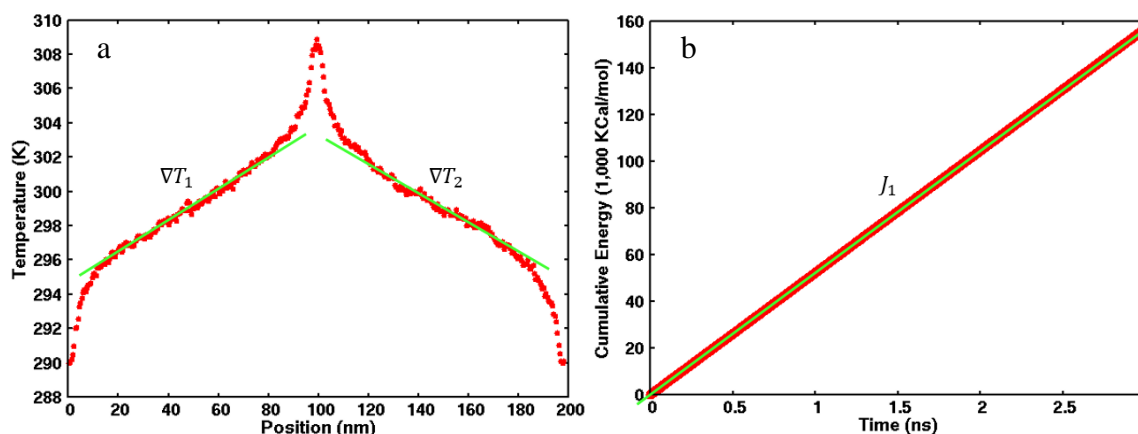
Figure 2.4: (a) Temperature profile from a Müller-Plathe simulation showing the linear fits of the temperature gradients. (b) Cumulative energy transferred from the cold bin to the hot bin in the Müller-Plathe simulation, along with the line of best fit to calculate the rate of heat flow.

CHAPTER 3: ANALYSIS OF SIMULATION METHODS USING Si

Before applying these simulation methods in new research to calculate the thermal conductivity of less studied materials and systems, it is necessary to establish the validity of each simulation method. By using each method to calculate the thermal conductivity of Si as a thin film and as a nanowire, the methods can be compared to well-established research on nanoscale heat transport in Si, and can also be compared and contrasted with one another to identify each method's inherent strengths and weaknesses. Comparing the results of each simulation method can also provide further insight into nanoscale thermal transport phenomena.

3.1 The Stillinger-Weber Potential

As MD simulations require interatomic potentials to model the properties of materials, several potentials have been developed for Si. One of the most popular models is the Stillinger-Weber (SW) potential. The SW potential accurately reproduces numerous properties of Si including melting point,[30] heat capacity,[31] elastic constants,[32] yield strength,[33] and thermal expansion coefficients.[19] Overall, it is one of the best MD models for Si available. The SW potential parameterizes the interatomic potentials of Si atoms using two terms: a two-body term that models the potential between two Si atoms as a function of the distance between them, and a three-body term that models the potential between three atoms as a function of both the distances between them as well as the angle they form. This three body term is crucial in modeling Si because of the directionality of the Si bonds in the diamond structure. The equations and parameters of the SW potential of Si are given in Table 3.1.[34-36]

Table 3.1: The equations and parameters of the Stillinger-Weber interatomic potential for Si.

Equations	
Stillinger-Weber Interatomic Potential	$$V(\boldsymbol{r}) = \sum_i \sum_{j>i} V_2(\boldsymbol{r}_{ij}) + \sum_i \sum_{j>i} \sum_{k>j} V_3(\boldsymbol{r}_{ij}, \boldsymbol{r}_{ik}, \cos\theta_{ijk})$$
Two-Body Term	$$V_2(\boldsymbol{r}_{ij}) = \begin{cases} A\varepsilon\left(B\left(\dfrac{\sigma}{\boldsymbol{r}_{ij}}\right)^p - \left(\dfrac{\sigma}{\boldsymbol{r}_{ij}}\right)^q\right) e^{\frac{\sigma}{r_{ij}-a\sigma}}, & r < a \\ 0, & r \geq a \end{cases}$$
Three-Body Term	$$V_3(\boldsymbol{r}_{ij}, \boldsymbol{r}_{ik}, \cos\theta_{ijk}) = \lambda\varepsilon e^{\frac{\gamma\sigma}{r_{ij}-a} + \frac{\gamma\sigma}{r_{ik}-a}}\left(\cos\theta_{ijk} + \frac{1}{3}\right)^2$$
Parameters	
A	7.049556277
B	0.6022245584
ε	2.17 eV = 50.0 Kcal/mol
σ	0.20951 nm
p	4
q	0
a	1.8
λ	21.0
γ	1.2

3.2 Simulation Details

The thermal conductivity simulations for this research were performed using the LAMMPS Molecular Dynamics Simulator produced by Sandia National Laboratories. Setting up the MD simulations begins with the generation of an Si diamond lattice with a lattice parameter of 0.5437 nm, oriented such that heat would flow in the <100> direction. For simulations using the thermostat method, the length of the Si structure in the heat flow direction includes both the contacts and the channels. The length of the contacts was set to 9.8 nm (18 unit cells) for all simulations, but the length of the channels was varied from 9.8 nm (18 unit cells) to 150.1 nm (276 unit cells) so that size effects on the thermal transport properties of the material could be observed. The lateral dimensions of the Si structure were set to 5.4 nm by 5.4 nm (10 x 10 unit cells). In order to simulate Si thin films, periodic

boundary conditions were applied in all directions, but for Si nanowires, the lateral dimensions were set to shrink-wrapped boundary conditions. The boundary conditions in the heat flow direction was set to periodic for both thin film and nanowire simulations. Because thermal conductivity is temperature dependent, the hot and cold contacts were thermostatted to 305 K and 295 K, respectively, so that the system would remain near room temperature. In order to expedite the system reaching steady-state heat flow, temperature gradients were generated within the channels at the start of the simulation by dividing each channel into a series of bins and gradually increasing the average velocity of the particles in each bin as they drew closer to the hot contact. The last step before beginning the simulation was to apply a thermostat to each of the contacts. When applying a thermostat in an MD simulation, the relaxation time must be specified. Using various thermostat relaxation times for the Nosé-Hoover and Langevin thermostats led to a significant result showing that the thermal conductivity can depend on the means of energy input into a system. This result is discussed in section 3.3.1. The relaxation times used in these simulations ranged from 1 fs to 50,000 fs in a logarithmic fashion. One distinction in the application of thermostats between the Nosé-Hoover and Langevin simulations is that the microcanonical ensemble (NVE) was applied to the entire simulation structure for the Langevin simulations, whereas it can only be applied to the channels, and not the contacts, in the Nosé-Hoover simulations, since the Nosé-Hoover thermostat yields the canonical ensemble (NVT). Once the simulation setup was complete, the simulations were run for 3 ns using a timestep of 1 fs.

The Müller-Plathe simulations use a similar simulation setup as the thermostat method, but because the Müller-Plathe method does not use thermostats, the contacts are removed from the simulation structure. The resulting structure is made up of two channels, and simulations were ran with channels lengths ranging from 9.8 nm to 150.1 nm. To produce an appropriate heat flow rate, the Müller-Plathe swap rate was set to occur once every 10 fs. The microcanonical ensemble was applied to the entire simulation structure, and the simulation was run for 3 ns with a timestep of 1 fs.

To calculate the temperature gradient in both simulation methods, the Si structure was divided into bins 1 unit cell in length in the heat flow direction. The temperature of each bin was calculated by averaging the kinetic energy of the particles within the bin and converting to Kelvin. The temperature profile was then produced by averaging the

instantaneous temperature of each bin, outputted every 0.5 fs, over the final 2 ns of the simulation. Checking to ensure the simulation had reached steady-state could be done in two ways, either by plotting the time evolution of the temperature of a few of the bins and determining when they begin to fluctuate around a constant value, or by plotting the cumulative energy output by the thermostats or the Müller-Plathe swapping and determining when it begins to increase in a linear manner (Fig. 3.1).
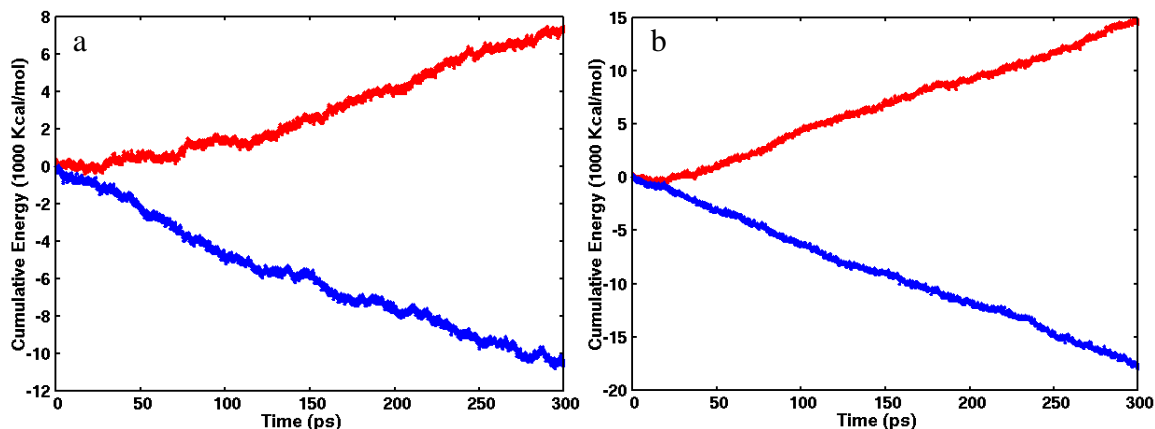
Figure 3.1: The first 300 ps of the cumulative energy input by the (a) Nosé-Hoover and (b) Langevin thermostats for simulations of an Si thin film with thickness of 50 nm. For the Nosé-Hoover simulation, steady-state at around 150 ps, and for the Langevin simulation, steady-state is achieved at around 30 ps.

3.3 Results and Discussion

3.3.1 Effects of the Thermostat Relaxation Time

This analysis of the thermal conductivity simulation methods will begin by comparing the performances of the two thermostats used in the thermostat method. Using an Si structure with a channel length of 50 nm, simulations were run with thermostat relaxation times varying from 1 fs to 50,000 fs in a logarithmic fashion. Fig. 3.2 shows the resulting thermal conductivity, heat flux, and temperature gradient as a function of relaxation time for each thermostat. Of primary interest in these plots is that, first, the Nosé-Hoover thermal conductivity results are independent of the relaxation time for values less than 10,000 fs, whereas the Langevin values are heavily dependent on the thermostat relaxation time.

Second, depending on the relaxation time, the thermal conductivity values from the Langevin simulations can be up to three times greater than the corresponding Nosé-Hoover value.
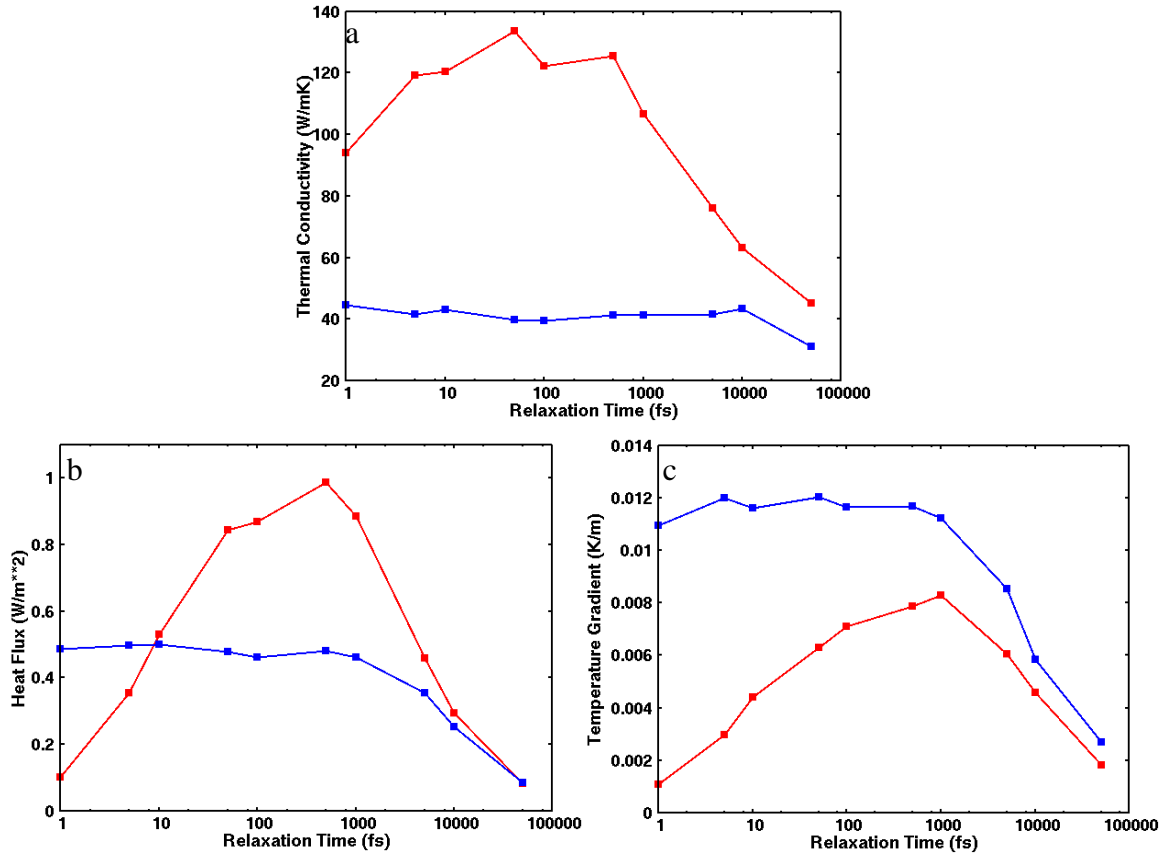
Figure 3.2: (a) Thermal Conductivity, (b) heat flux, and (c) temperature gradient as a function of thermostat relaxation time for 50 nm Si thin films using the Langevin (red) and Nosé-Hoover (blue) thermostats.

The first step towards understanding the dependence of thermal conductivity on relaxation time will be to examine the decrease in values for both thermostats once the relaxation time becomes sufficiently large. As can be seen in Fig. 3.2b and 3.2c, the heat flux and temperature gradient values for both thermostats begin to decrease at around relaxation time of 1,000 fs. The reason for these decreasing values can be revealed by analyzing the temperature profiles for these simulations, which are depicted in Fig 3.3. These profiles reveal that, at sufficiently large relaxation times, the temperature difference between the contacts decreases because energy is flowing out of the contacts faster than the thermostats

can correct the change. As such, the heat flux and temperature gradient values will begin to decrease. Despite these decreasing values, the Nosé-Hoover thermal conductivity results remain constant up until a relaxation time of greater than 10,000 fs. The Nosé-Hoover thermal conductivity will begin to drop below its constant value once the relaxation time becomes large enough that the simulation structure essentially reaches thermal equilibrium between successive thermostat temperature adjustments. As a result, the thermal conductivity begins dropping towards zero.
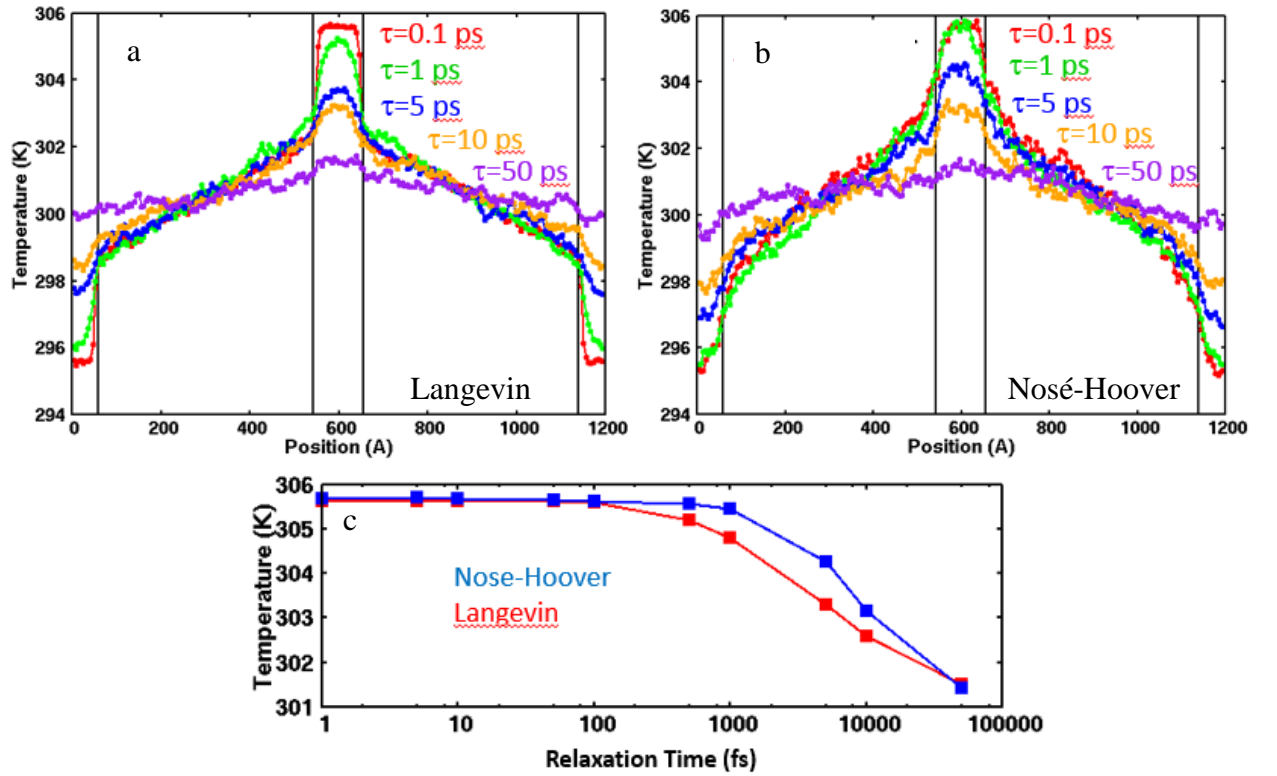
Figure 3.3: Temperature profiles generated using the (a) Langevin and (b) Nosé-Hoover thermostats with varied relaxation times, along with (c) a plot of temperature of the hot contact vs relaxation time for the two thermostats.

Of more significance than the effects of the failing thermostats, which explains the decrease in thermal conductivity for larger relaxation times, is why the Langevin thermostat does not give consistent thermal conductivity values for relaxation times low enough to maintain the contacts at their respective temperatures. If the contacts are kept at constant temperatures for lower thermostat relaxation times, which is demonstrated in Fig. 3.3c, then

the expected result would be consistent thermal conductivity values. This expected result is observed with the Nosé-Hoover thermostat, but it does not occur with the Langevin thermostat. Instead, the Langevin results decrease as the relaxation times become smaller. Since the thermal transport in these Si thin films occurs predominantly by phonons, the conclusion must be that the Langevin thermostat interacts with the phonons within the contacts in a way that the Nosé-Hoover thermostat does not. One means of analyzing the phonons within a material is to calculate the phonon density-of-states (PDOS). A PDOS maps the number of phonons present in a material according to their respective energies. Because atomic vibrations are influenced by the lattice structure and atomic bonds, certain phonon energies are more likely to occur than others, causing them to show up as a peak in the PDOS. PDOSs can be generated from MD simulations via a fast Fourier transform method that uses a periodic output of the position and velocity of every atom in the simulation structure. The PDOSs of thermostatted and unthermostatted Si given in Fig. 3.4 for various relaxation times were calculated by outputting the position and velocity of the atoms every 20 fs over the course of 8,000 fs.
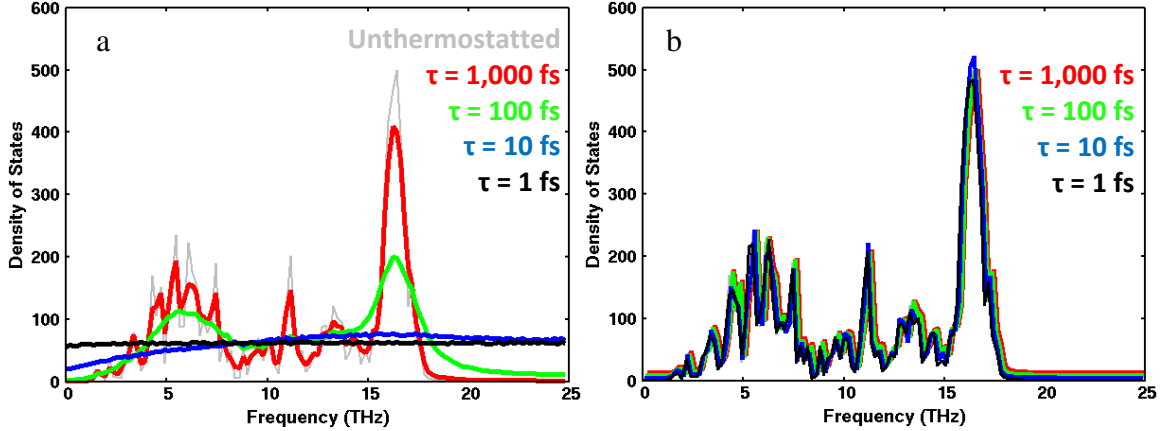
Figure 3.4: Phonon density-of-states for Si under (a) Langevin and (b) Nosé-Hoover thermostats using relaxation times of 1, 10, 100, and 1,000 fs. The PDOS of unthermostatted Si is shown in gray in the Langevin plot, and the Nosé-Hoover PDOS curves are slightly offset to make visualization easier.

The PDOSs of thermostatted Si reveal that the Langevin thermostat does, in fact, affect the phonons of Si, whereas the Nosé-Hoover thermostat has no influence on Si's normal phonon modes. Furthermore, the lower the relaxation time of the Langevin

thermostat, the greater of an impact it has on the PDOS. For very low relaxation times (< 10 fs), the PDOS becomes nearly flat, signifying that the phonons are uniformly distributed by energy. But, as the relaxation time increases, the PDOS gradually takes the form of thermostatted Si. A model for how the Langevin thermostat disrupts the normal phonon modes of Si can be developed using the theory behind the thermostat. As described in section 2.3.2, the Langevin thermostat controls the temperature by placing the atoms in a fictitious solvent. The temperature of the solvent is kept at the target temperature, which then keeps the thermostatted atoms at the same temperature through fictitious collisions. These collisions are randomized in their direction and force, meaning that they affect the normal vibrational patterns of an Si atom every time a collision occurs. Decreasing the relaxation time of thermostat increases the rate of collisions, causing a greater disruption in atomic vibrations. In this manner, the normal phonons of Si are greatly affected by a strong Langevin thermostat. The Nosé-Hoover thermostat does not affect atomic vibrations because it works by adjusting the energy of the thermostatted atoms, which has no effect on their vibrational patterns. The peak in the Langevin thermal conductivity results is therefore at the point in which the phonons are not as disrupted as they are under a strong thermostat, because the collisions with the fictitious solvent atoms lower the phonon mfp. Curiously, however, the Langevin thermostat results in a much higher thermal conductivity than when using the Nosé-Hoover thermostat. This increase in thermal conductivity could be due to an increase in the number of low frequency phonons, which are not as easily scattered, and which contribute more to the total thermal conductivity than high frequency phonons. Although the exact reason for the higher thermal conductivity when using the Langevin thermostat has not been confirmed, these results reveal that the means of energy input into a material can affect its thermal transport properties. Such a result provides an additional means of controlling the thermal properties of a system, which is useful when precise thermal control is needed to optimized the performance of a nanotech device.
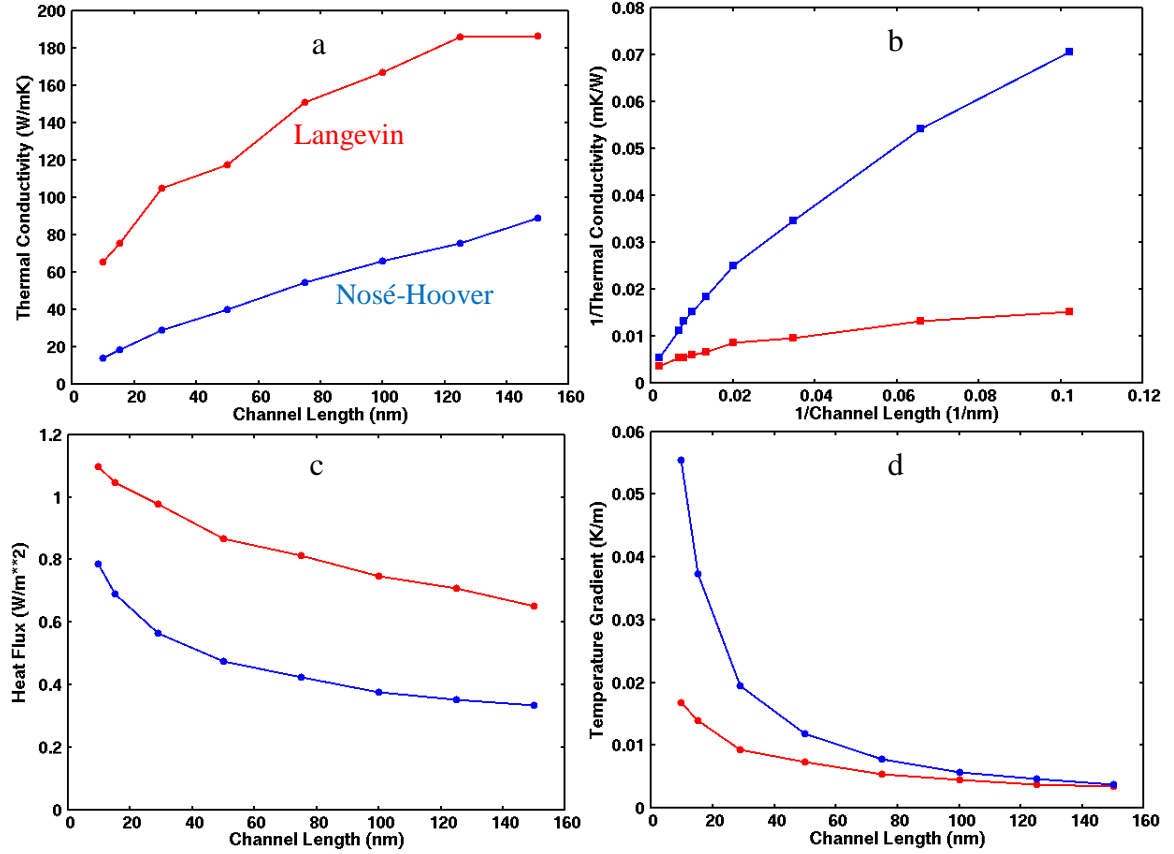
Figure 3.5: (a) Thermal conductivity vs channel length, (b) inverse thermal conductivity vs inverse channel length, (c) heat flux vs channel length, and (d) and temperature gradient vs channel length of thin film Si from thermostat method NEMD simulations using the Langevin (red) and Nosé-Hoover (blue) thermostats. Fig. b includes an additional data point that corresponds to a channel length of 500 nm.

3.3.2 Thermal Conductivity of Si Thin Film

An understanding of the effects of thermostat relaxation time on thermal conductivity provides the proper context for analyzing further simulation results. Of chief interest is the dependence of thermal conductivity on the channel length of the simulation structure. Fig. 3.5 shows the changes in thermal conductivity, heat flux, and temperature gradient as a function of channel length for Si thin films, calculated using the Langevin and Nosé-Hoover thermostats. As depicted, the heat flux (Fig. 3.5c) and temperature gradient (Fig. 3.5d) of the thin films decrease with increasing film thickness, but for very short channel lengths, the values begin to rise dramatically, especially for the Nosé-Hoover thermostat. These results

make sense considering the impact of the contact temperature, which, for short channel lengths, will spur a large temperature gradient and a high rate of heat flow. The steeper rise in the Nosé-Hoover values is due to the ability for temperature gradients to form within the contacts, which interact with the temperature gradients of the channels. The Langevin thermostat can support lower temperature gradients for short channel lengths due to the phonon mismatch at the contact-channel interfaces that cause larger temperature jumps to form. Because the contacts primarily influence the dynamics of the simulation structure near their respective locations, their effects should lessen as the channel length is increased, which corresponds to the results, particularly as seen in Fig. 3.5b, which displays inverse thermal conductivity vs inverse channel length and includes an additional point corresponding to a channel length of 500 nm. The ability of NEMD simulations to study even shorter channels lengths than 10 nm is limited since the channel length will become only a few atoms thick, and having so few atoms contributing to the calculations makes it challenging to produce meaningful values for the heat flow rate and temperature gradient.

At the longer channel lengths, the temperature gradients for each thermostat method converge, but the Langevin heat flux is still double the Nosé-Hoover value. Consequently, the greater Langevin thermal conductivity comes solely through a greater heat flux, with the temperature gradient contributing nothing to the difference once the channel length reaches 150 nm. As a result, the Langevin thermostat, through the way it affects the normal phonon modes of Si, results in a thermal conductivity twice that of the Nosé-Hoover simulation at a channel length of 150 nm. Furthermore, the increasing trend in thermal conductivity with increasing channel length corresponds to current phonon heat transport theory. A thin film longer channel length allows for a greater phonon mfp, which allows heat carrying phonons to travel farther before scattering. At sufficiently large channel lengths, the thermal conductivity should plateau at the bulk value, because the phonon mfp will no longer be limited by the channel length. The thermal conductivity of bulk Si can be estimated using the thin film results by using a linear extrapolation method on the inverses of the channel length and thermal conductivity. Bulk Si can be considered as a thin film with infinite thickness, which corresponds to a thin film with an inverse channel length of zero. Therefore, by taking a linear fit of inverse thermal conductivity to inverse channel length, the y-intercept will yield an estimation of the bulk value. This process is depicted in Fig. 3.6, which includes

data form Müller-Plathe simulations that were performed by research group member Edwin Antillon. The resulting thermal conductivity values for bulk Si are 317.0, 322.7, and 339.0 W/mK for the Langevin, Nosé-Hoover, and Müller-Plathe methods, respectively. The convergence of the Langevin and Nosé-Hoover results further supports the conclusion that the thermostat effects occur only on the nanoscale.
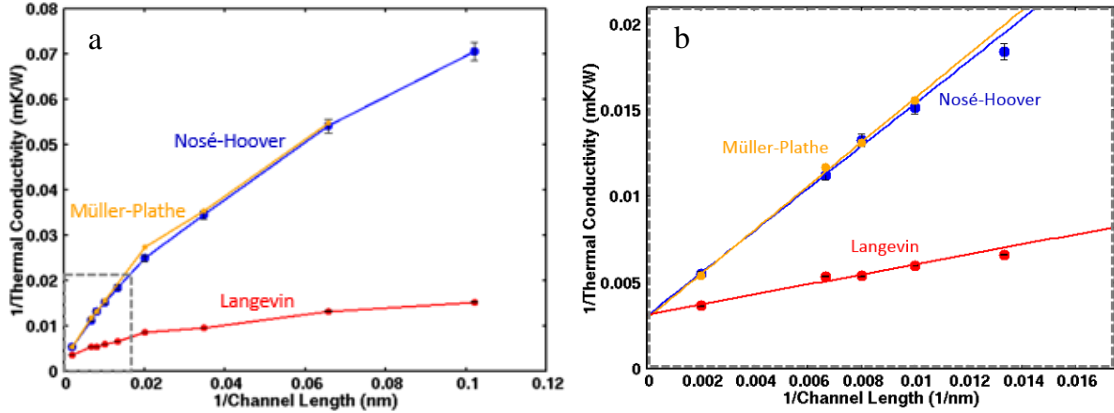
Figure 3.6: (a) Inverse thermal conductivity as a function of inverse channel length for thermostat method NEMD simulations using the Langevin (red) and Nosé-Hoover (blue) thermostats, as well as results from Müller-Plathe method (yellow) simulations. (b) A zoomed-in portion of the plot to demonstrate the convergence of the three simulation types.

In comparison to other published values on the thermal conductivity of Si, the Nosé-Hoover thermostat gives much closer values than the Langevin thermostat. Zhang and Sun report a MD thermal conductivity value of an Si thin film with thickness of 23 nm to be around 23 W/mK,[37] which matches very well with the Nose-Hoover value of around 26 W/mK. Sellen and Turney *et. al.* used three different lattice Boltzmann approximation methods in their calculations and reported values of 67.9, 53.1, and 67.8 nm for an Si film with thickness of 100 nm,[38] which correspond to the Nose-Hoover result of about 61 W/mK. Using the Boltzmann transport equation, Jeong, Datta, and Lundstrom predicted a value of 70 W/mK for the same film thickness.[39] For the extrapolation to bulk values, the estimated thermal conductivities are 317.0, 322.7, and 339.0 W/mK. Volz and Chen report a lower value of 250 W/mK using the Green-Kubo method,[40] whereas the experimental value is 150 W/mK. However, it is well-established that the Stillinger-Weber potential overestimates the thermal conductivity of Si.[38]
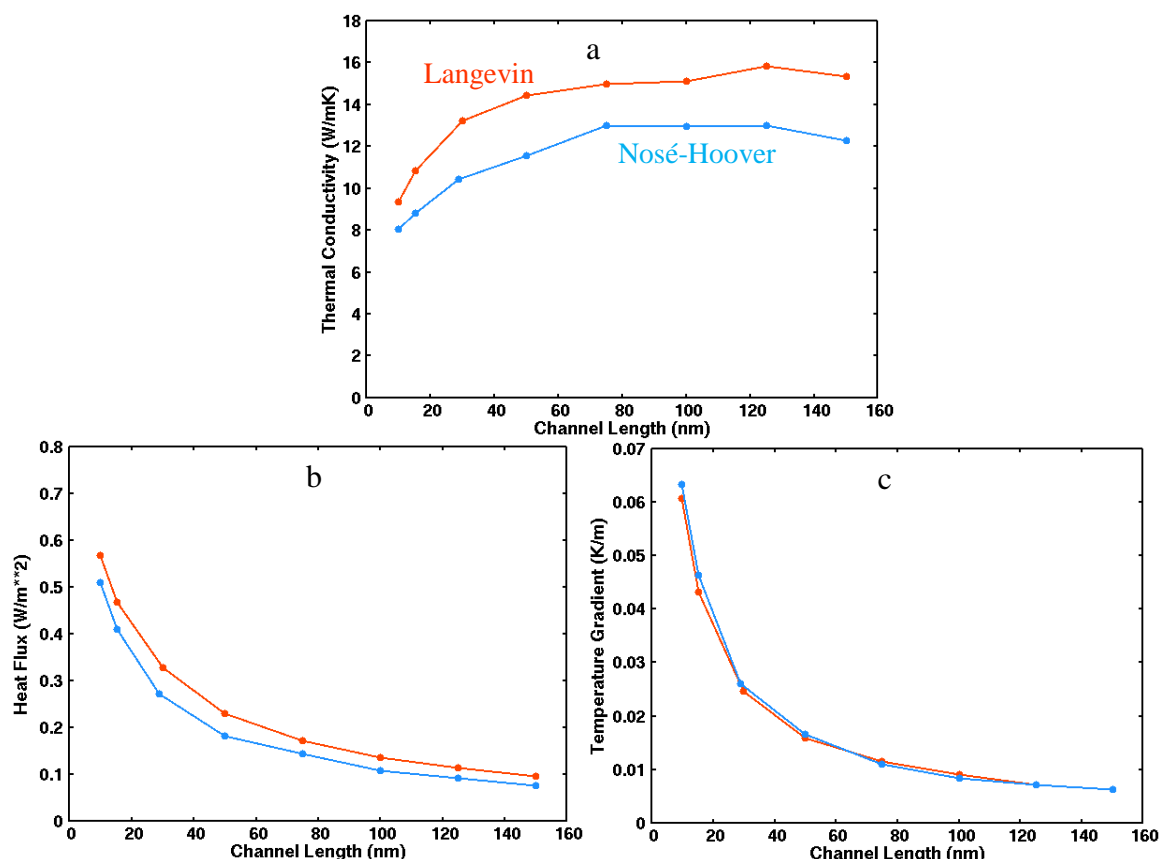
Figure 3.7: (a) Thermal Conductivity, (b) heat flux, and (c) temperature gradient as a function of channel length of Si nanowires using the Langevin (orange) and Nosé-Hoover (light blue) thermostats.

3.3.3 Thermal Conductivity of Si Nanowires

In addition to examining Si thin films, the size dependence of thermal conductivity for Si nanowires was also analyzed, the results of which are given in Fig. 3.7. The differences between the Langevin and Nosé-Hoover thermostats are much less pronounced for Si nanowires. Whereas the Langevin results were up to four 4 times greater than Nosé-Hoover for Si thin films, they are only 1.5 times greater for nanowires. The thermal conductivity values themselves are 10-fold lower than those calculated for thin films, dropping from around 100 W/mK to about 10 W/mK. The plots for heat flux and temperature gradient look very similar for Nosé-Hoover and Langevin. The temperature gradients are nearly identical for every channel length, and the Langevin heat flux values are only slightly higher than the ones for Nosé-Hoover. Whereas the Langevin temperature gradient does not rise dramatically at shorter channel lengths for thin films, it does for

nanowires. An interesting facet is that the thermal conductivity values for both thermostats seem to plateau at channel lengths greater than 80 nm, which indicates that the low dimensionality limits the phonon mfp from increasing any further at such channel lengths. These thermal conductivity values are on the same order of other published results. Yang, To, and Tian produced results of 5.5 W/mK for 50 nm channel length and 8 W/mK for 150 nm, which are slightly less than the Nosé-Hoover results of 11 and 12 W/mK, respectively.[42]
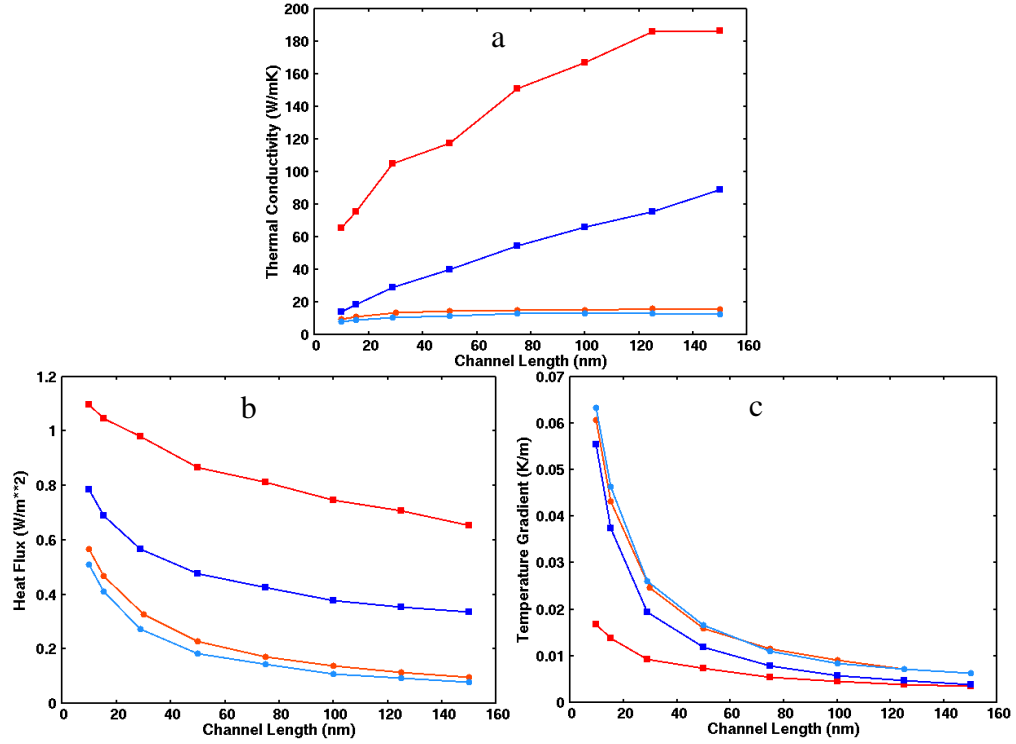
Figure 3.8: A comparison of (a) thermal conductivity, (b) heat flux, and (c) thermal conductivity as a function of channel length for Si thin films (squares) and nanowires (circles) using the Langevin (red and orange) and Nosé-Hoover (blue) thermostats.

3.3.4 Comparison between Si Thin Films and Nanowires

Fig. 3.8 provides a comparison between thermal conductivity, heat flux, and temperature gradient for Si thin films and nanowires. The nanowire temperature gradients are only slightly greater than the values for Nosé-Hoover thin films, making the dramatic difference in thermal conductivity between thin film and nanowires primarily dependent on the heat flux. The nanowire heat flux values range from 1.5 to 5 times lower than the Nosé-

Hoover thin film values, resulting in much lower thermal conductivity values. This result, again, fits with phonon heat transport theory since the surfaces of the nanowires limit the phonon mfp. In fact, the plots for nanowire thermal conductivity plateau very quickly, in contrast to the steadily increasing thin film values, indicating that the phonon mfp has such a strong dependence on the dimensions of the nanowire that increasing the channel length beyond around 80 nm has little effect on it. Fig. 3.9 demonstrates the effects of increasing the cross-sectional area of the Si nanowires. The heat flux, temperature gradient, and thermal conductivity values are plotted against the inverse of the cross-sectional area so that the thin film value—which corresponds to a nanowire with infinite cross-section area—can be plotted at zero. As expected, the thermal conductivity values gradually increase with increasing cross-sectional area, and the values look to be trending towards the thin film results. The thermal conductivity plot provides an excellent picture of how the difference between the Langevin and Nosé-Hoover results for thin films almost disappears as the Si structure transitions to a nanowire. Because of the wide range of thermal conductivity values obtained through varying the thickness of thin films or the cross-sectional area of nanowires, precise thermal conductivity values needed for specific device specifications can be engineered by choosing the appropriate size of material. This result demonstrates how research into nanoscale thermal transport can provide insight into how to overcome thermal problems in nanotechnology.
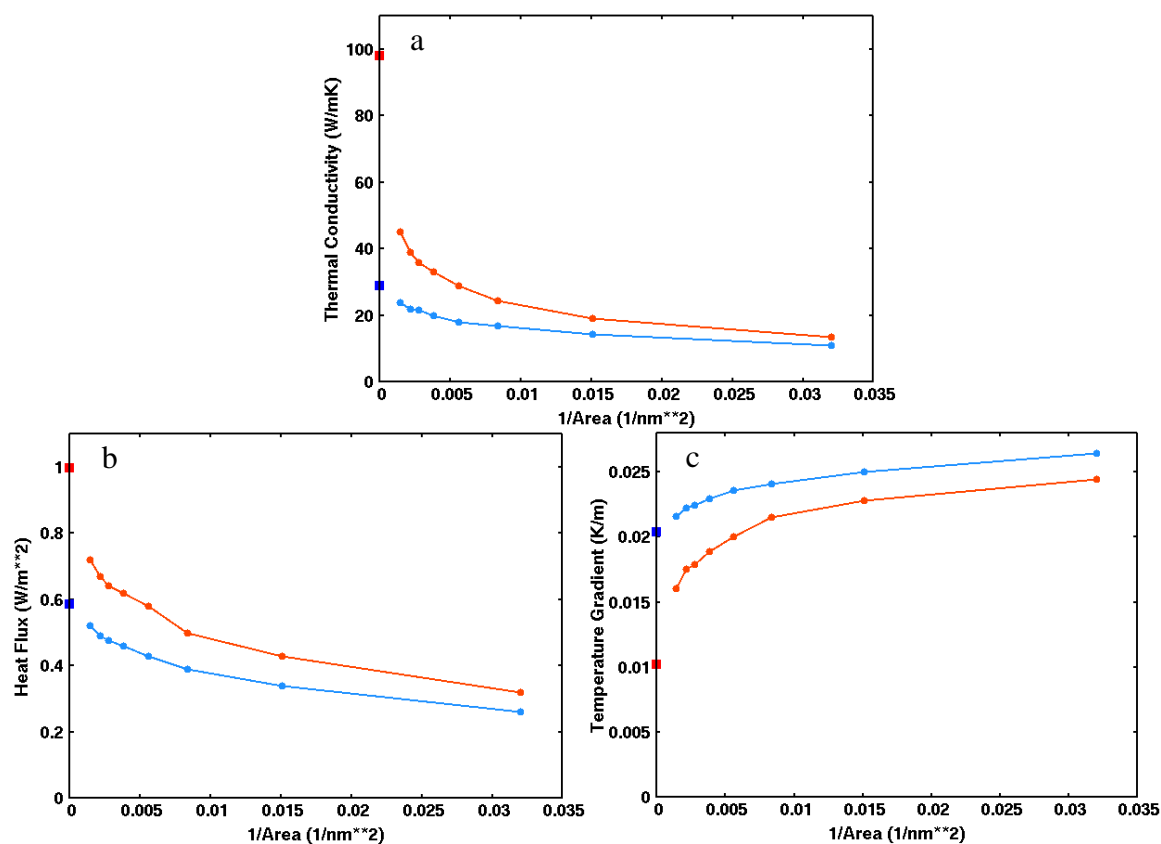
Figure 3.9: The effects of increasing the cross-sectional of Si nanowires on the (a) thermal conductivity, (b) heat flux, and (c) temperature gradient for simulations using the Langevin (orange) and Nosé-Hoover (light blue) thermostats. The values are plotted against inverse cross-sectional area to allow for the thin film value to be plotted at zero.

CHAPTER 4: THERMAL CONDUCTIVITY OF MoTe$_2$ AND MoTe$_2$Cu

4.1 Introduction

Having investigated the thermal conductivity simulation methods and gained a deeper understand of the factors that affect the MD simulation results, these calculation techniques were then used to investigate the thermal conductivities of novel and unique systems, the first of which were MoTe$_2$ and MoTe$_2$Cu. The Müller-Plathe approach was chosen to study these materials as its results match very closely to the Nosé-Hoover values (see Fig 3.6), but is the more well-known simulation method.

MoTe$_2$ belongs to a class of materials known as transition metal dichalcogenides (TMDs). TMDs are attracting much interest into today's scientific community because they form layered structures that, if isolated as a single layer, become what is called a two-dimensional (2-D) material due to its planar structure. Because of their low dimensionality, 2-D materials possess many unique properties that show promising applications in nanotechnology. Graphene, the most well-known 2-D material, shows extremely high electrical conductivity due to ballistic electron propagation[42] as well as incredible strength and stiffness.[43] Graphene is limited, however, in some applications due to its chemical inertness.[44] TMDs, on the other hand, cover a wide range of material properties because of the large variety of elements that can be paired together in the TMD structure. TMDs are characterized by the chemical formula unit of MX$_2$, where M is a transition metal (i.e. Mo, W, Ti, Nb, and V) and X is a chalcogen (S, Se, and Te). Depending on the choice of transition metal and chalcogen, TMDs can be metals (NbS$_2$ and VSe$_2$), insulators (HfS$_2$), semiconductors (MoS$_2$ and WS$_2$), or even superconductors (NbSe$_2$ and TaS$_2$),[44,45] and many of the properties found in bulk TMDs are retained when reduced to monolayers.[44]

Recent research has investigated the use of TMDs for a variety of applications including transistors, sensors, and photovoltaics.[46] TMDs also show promise in the

development of thermoelectric devices due to an inherently low thermal conductivity, high Seebeck coefficient,[47] and ZT values comparable to thin film Si.[48] $MoTe_2$, specifically, is a semiconducting TMD that uniquely undergoes a phase transition at high temperatures that changes it from being diamagnetic to paramagnetic.[49] $MoTe_2$ shows promise in such applications as opto-electronics and energy storage,[44] but the properties of $MoTe_2$ have not been researched as much as other TMDs, leaving much work still to be done. Specifically, no values for the thermal conductivity of $MoTe_2$ have yet been published. To further research efforts for $MoTe_2$, fellow research group member Nicolas Onofrio has developed a reactive force field for $MoTe_2$ and $MoTe_2Cu$, which has been applied in this work. Research into the properties of $MoTe_2Cu$ are just beginning, but it also holds potential in electronic applications.

4.2 Description of TMD Structure

As depicted in Fig. 4.1b, the structure of TMDs consists of a sheet of transition metal atoms bonded to two sheets of chalcogen atoms. Together, the bonded atoms form a hexagonal lattice (Fig 4.1c). Depending on the bonding orientation of the transition metal, the TMD structure can take on one of two forms. A trigonal prismatic orientation (Fig. 4.1a) gives rise to the H-phase, and a trigonal anti-prismatic orientation (Fig. 4.2a) gives rise to the T-phase (Fig 4.2).[50] Whereas the atoms within each layer are held together by strong covalent bonds, the layers themselves hold together through weak Van der Waals interactions. As such, layers of TMDs are easily separable, and monolayers can obtained by such methods as liquid exfoliation.[51]
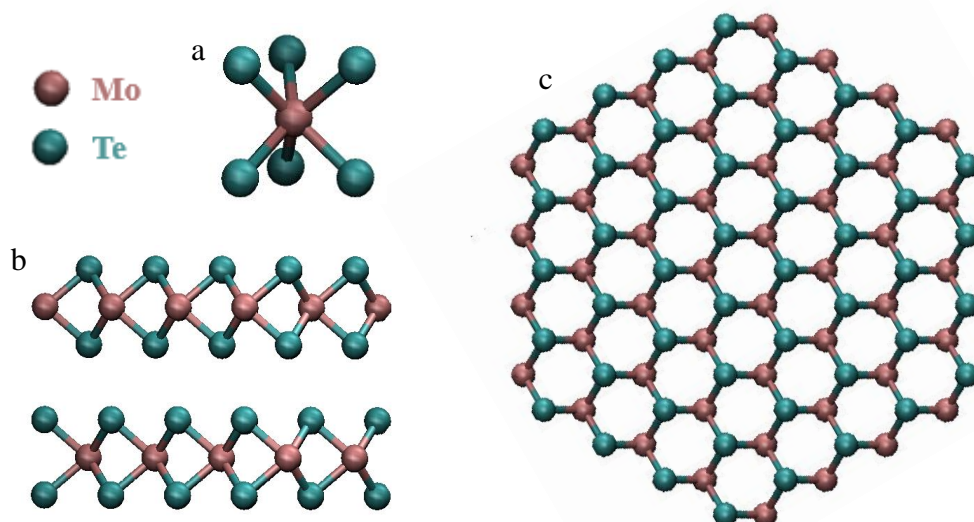
Figure 4.1: The H-phase of MoTe$_2$, depicting (a) the trigonal prismatic orientation of the bonds, (b) the layered structure viewed from the side, and (c) the hexagonal lattice viewed from above a layer.
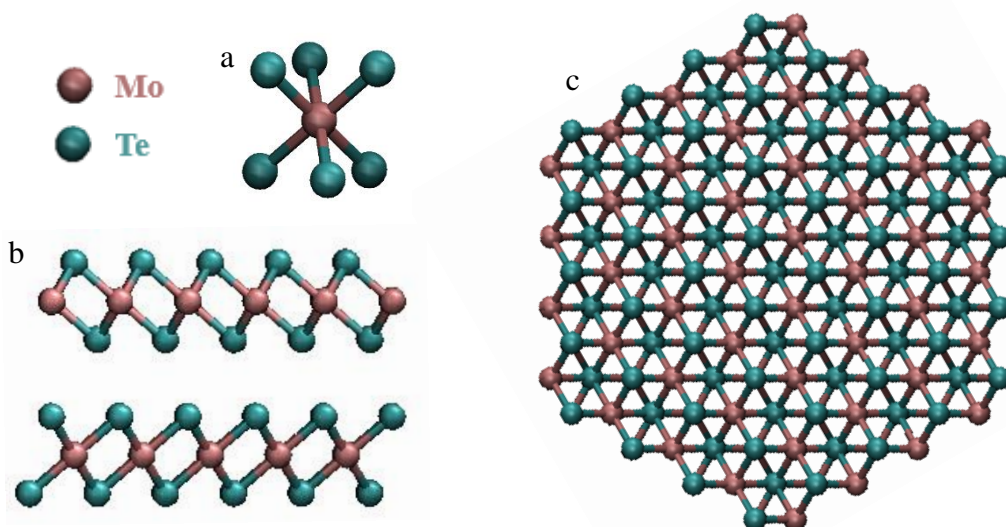
Figure 4.2: The T-phase of MoTe$_2$, depicting (a) the trigonal anti-prismatic orientation of the bonds, (b) the layered structure viewed from the side, and (c) the hexagonal lattice viewed from above a layer.

Because of the layered structure of TMDs, dopant atoms, which are usually a transition metal, can be added between the layers to form intercalated TMDs, which will have modified properties over the pure TMD structure. Since the dopant affects the properties of the material, its exact concentration can be adjusted to control a desired property. In this study, the H-phase of MoTe$_2$ is used in all simulations, as it is the more

stable phase at room temperature.[50] Cu is then added as a dopant to produce Cu-intercalated MoTe$_2$ (MoTe$_2$Cu) to analyze the resulting changes in thermal conductivity. Although the Cu atoms are initially placed in the octahedral sites between subsequent MoTe$_2$ layers, they are able to move around in the space between the MoTe$_2$ layers. The concentration of Cu can be defined in terms of the percentage of octahedral sites between MoTe$_2$ layers initially occupied by a Cu atom. For example, in a 2x2x1 supercell of MX$_2$ there are eight octahedral sites between the layers in which a Cu atom can be positioned. Adding one Cu atom at a time produces Cu concentrations ranging from 0.125 to 1, which are the concentrations used in this study. Because MoTe$_2$ has a layered structure, its thermal conductivity is anisotropic. As such, an important result will be an analysis of how Cu atoms affect the not only the lateral thermal conductivity, but also the transverse thermal conductivity.
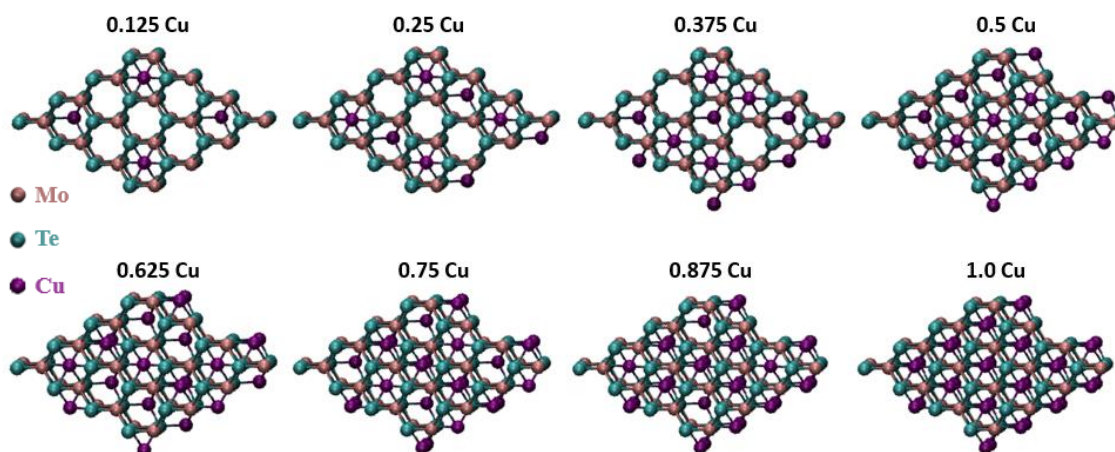
Figure 4.3: Portions of a Cu-intercalated MoTe$_2$ structure, with the Cu concentration determined by the percentage of H-sites in between the layers of MoTe$_2$ that are occupied by a Cu atom.

4.3 Simulation Design

Because this research was performed during the development of a MoTe$_2$ force field, several different preliminary force fields were tested to see how they performed in thermal conductivity calculations. Two of the force fields were created using Mulliken charge analysis and two using Bader analysis. Mulliken charge analysis uses atomic orbitals to calculate the charge on each atom. The charge assigned to each atom is the same charge used

in the basis function for that atom when determining the electronic wavefunction of the system. Bader charge analysis instead uses the charge density of the system to determine the charge on each atom. It divides the system into regions defined by planes that pass through minima in the charge density. Each region will contain 1 or 0 atomic nuclei. The charge of an atom is then calculated by integrating the charge density of its region, with possible inclusion of surrounding empty regions depending on the exact type of calculation method.[52] Because no values for the thermal conductivity of $MoTe_2$ have yet been published, the comparison between these force fields provides a wider basis for understanding the results.

To run the simulations, the Müller-Plathe method was used with a timestep of 0.5 fs, a swap rate of once every 2,000 fs, and a total simulation run time of 1.5 ns. In order for steady-state to be achieved quickly, an initial temperature gradient from 250 K to 350 K was imposed on the simulation. The channel lengths, which were one-half of the total length of the simulation structure, ranged from 35.7 to 1426.4 nm (100 to 400 unit cells), with lateral dimensions of 2.2 nm (7 unit cells) along the layers and 5.7 nm (4 unit cells or 8 layers) in the stacking direction.

To study the effect of intercalated Cu on $MoTe_2$ thermal conductivity, the Cu concentration was varied in a series of simulations, each with a channel length of 71.3 nm (200 unit cells). The swap rate for these simulations was set to once every 4,000 fs. Additionally, the effect of Cu-dopant on the thermal conductivity in the transverse direction was studied by creating a simulation structure 283.2 nm (200 unit cells) in the stacking direction and 2.9 x 2.9 nm (8 x 8 unit cells) along each layer. These simulations used a timestep of 0.5 fs, a swap rate of once every 4000 fs, and a total simulation run time of 1.5 ns.

4.4 Results and Discussion

4.4.1 Thermal Conductivity of $MoTe_2$

The first step in establishing MD thermal conductivity values for $MoTe_2$ is to test the reliability of each of the force fields in comparison to experimental and DFT results. Table 4.1 displays the lattice parameters of a relaxed $MoTe_2$ structure simulated using each force

field. The Bader 1 force fields produces the closest lattice parameters to DFT and experimental results, while the Mullikan 2 force field yields the largest difference. More importantly than the lattice parameters, however, is how the phonon density of states (PDOS) of each force field compares to DFT results, which is displayed in Fig. 4.4 using a phonon dispersion curve from a DFT simulation. Because phonon thermal conductivity is dominated by low frequency phonons, the lowest region of the PDOSs are the most relevant when analyzing the ability of the force fields to produce reliable values. As can be seen, the lower peaks of each PDOS falls below the frequencies of the lower bands in the DFT phonon dispersion curves. Consequently, it would be expected for each of the force fields to underestimate the thermal conductivity of $MoTe_2$, with the Mullikan 2 force field producing the highest results and the Bader 2 force field producing the lowest.

Table 4.1: Lattice parameters of $MoTe_2$ for each force field with a comparison to DFT and experimental results. The $MoTe_2$ unit cell covers two layers with three atoms in each layer. Lattice parameter a is in the across-layer direction, and lattice parameter c describes the lateral dimensions.

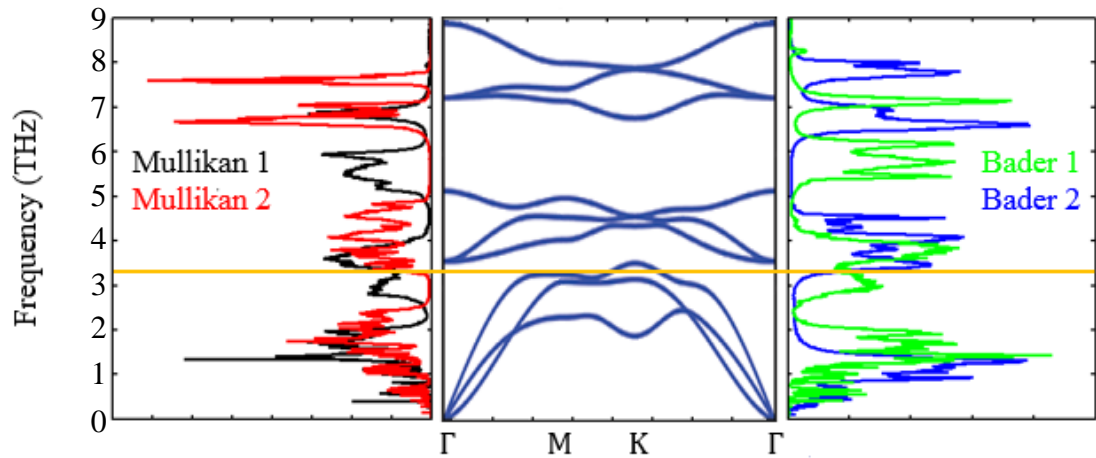| Lattice Parameters	Expt.[53]	DFT[45]	Mullikan 1	Mullikan 2	Bader 1	Bader 2
a	0.351 nm	0.354 nm	0.346 nm	0.382 nm	0.349 nm	0.373 nm
c	1.397 nm	1.395 nm	1.420 nm	1.273 nm	1.388 nm	1.301 nm

Figure 4.4: PDOSs of the four preliminary $MoTe_2$ force fields used in the thermal conductivity simulations: Mullikan 1 (black), Mullikan 2 (red), Bader 1 (green), Bader 2 (blue). The phonon dispersion curve used data from Ref. 50 and was calculated using DFT. The yellow line marks the top of the lowest frequency bands, which contribute the most to thermal transport.

The thermal conductivity of $MoTe_2$ as a function of channel length using each of the $MoTe_2$ force fields is displayed in Fig. 4.5. As expected from the PDOSs, the Mullikan 2 force field produces the highest results, and the Bader 2 force field produces the lowest results. The differences between the curves gives a good picture of how much the thermal conductivity values vary with changes in the PDOS. Because the thermal conductivity values fall within a range 3 W/mK for each channel length, then the results for a PDOS that was better aligned with the phonon dispersion curve should not vary more than a few W/mK from these results. For the same range of channel lengths, the thermal conductivity of Si thin films using the Nosé-Hoover thermostat increased from 10 to 80 W/mK. Therefore, it is clear that the thermal conductivity of $MoTe_2$ is much lower than Si, which makes it a promising thermoelectric material since the thermoelectric efficiency increases with decreasing thermal conductivity.
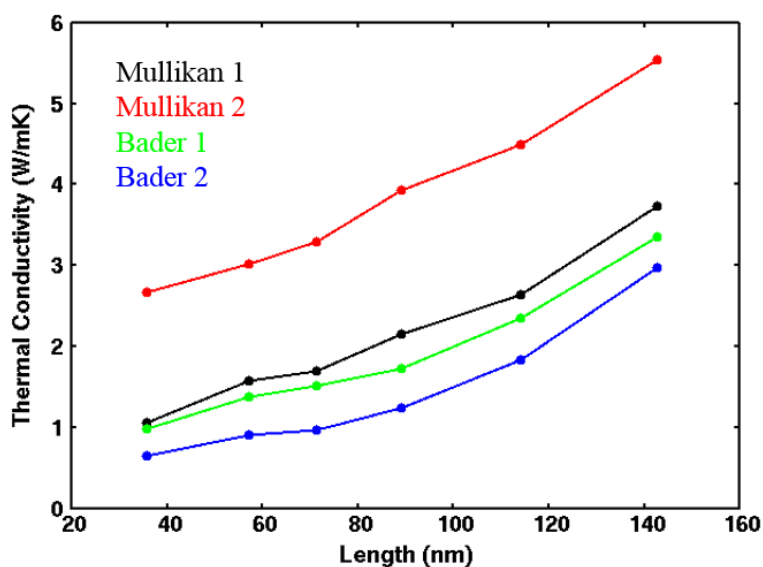
Figure 4.5: Thermal conductivity vs channel length for $MoTe_2$ simulating using force fields developed using Mullikan (black and red) and Bader (green and blue) charge analysis.

Since no values for the thermal conductivity of $MoTe_2$ have yet been published, the results from these MD simulations will be compared with published experimental thermal conductivity values for MoS_2 and $MoSe_2$. Kim, *et. al.* performed a laser flash technique to calculate the thermal conductivities of bulk MoS_2 and $MoSe_2$, with results of 1.05 W/mK

and 0.85 W/mK, respectively.[54] Kumar and Schwingenschlogl report a slightly higher MoSe$_2$ result of 2.3 W/mK.[46] From these results, it can be predicted that MoTe$_2$ thermal conductivity will also fall on the order of only a few W/mK, which is on par with these results.

4.4.2 Thermal Conductivity of MoTe$_2$Cu

One of the most promising features of MoTe$_2$ regarding its application in nanotechnology is its ability for a transition metal to be intercalated between the layers of its atomic structure. The intercalation of Cu into the MoTe$_2$ structure and its effects on thermal conductivity both along the layers and across the layers is analyzed in this research. To begin, Fig.4.6 shows the effect of the Cu intercalation on the PDOS of MoTe$_2$ for various concentrations of Cu. As can be seen from the PDOSs, the intercalated Cu has an impact on the phonons of the MoTe$_2$ structure, but the thermal conductivity simulations need to be performed to learn in what way it affects its thermal properties.

Figure 4.6: The PDOS of MoTe$_2$Cu for Cu concentrations of 0.125 (red), 0.375 (green), 0.625 (blue), and 0.875 (purple).

Fig. 4.7a plots thermal conductivity along the layers of Cu-intercalated MoTe$_2$ as a function of Cu concentration. The MoTe$_2$Cu structures at various concentrations of Cu can be seen in Fig. 4.3. These results indicate that adding a small amount of Cu between the
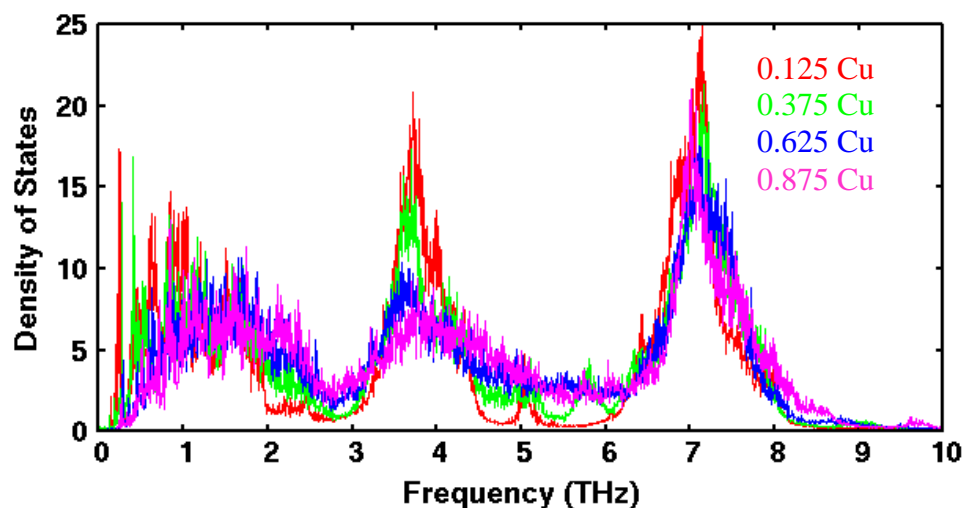
layers of MoTe$_2$ significantly decreases the thermal conductivity, while increasing the Cu concentration will gradually bring the thermal conductivity back up to undoped levels. The decrease in thermal conducting for small concentrations in Cu can be attributed to the disruptions in the normal phonon modes created by the small number of Cu atoms. As the Cu atoms move around between the layers of the MoTe$_2$ structure, they will only be interacting with a small fraction of the MoTe$_2$ atoms. In this way, the will be affecting the vibration modes of some, but not all, of the MoTe$_2$ atoms. The inconsistent influence causes disruptions in the propagation of phonons through the material and, consequently, lowers the thermal conductivity. As the Cu concentration increases, the number of MoTe$_2$ atoms that interact with the Cu atoms at every moment increases, which makes the vibrational modes of the simulation structure as a whole more consistent. The greater consistency in vibrational modes causes fewer disruptions to the propagation of phonons through the material and results in a greater thermal conductivity. The thermal conductivity of fully-doped MoTe$_2$ is just below the thermal conductivity of undoped MoTe$_2$.
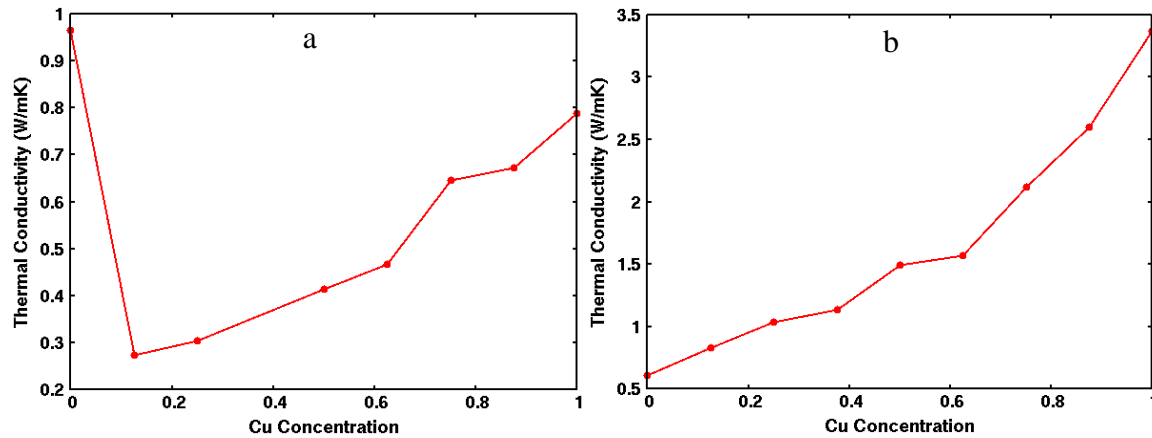
Figure 4.7: The (a) along the layers and (b) across the layers thermal conductivity of Cu-intercalated MoTe$_2$ as a function of Cu concentration.

The thermal conductivity across the layers of MoTe$_2$Cu, depicted in Fig. 4.7b, provides additional insight into means controlling its thermal properties. For an undoped MoTe$_2$ structure, the thermal conductivity across the layers is very low since the gaps between the layers prevent strong interaction between atoms in two different layers, greatly hindering phonons from traveling from layer to layer. The addition of intercalated Cu,

however, provides a bridge between the MoTe$_2$ layers along which phonons can travel from one layer to another. As a result, the thermal conductivity increases, and continues to increase for greater concentrations of Cu. The fully doped MoTe$_2$ structure allows for a large amount of phonons to propagate across the layers, and, in fact, the across layer thermal conductivity of MoTe$_2$Cu is 2 W/mK greater than its thermal conductivity along the layers.

The varying thermal conductivity of MoTe$_2$ due to its size and concentration of intercalated Cu provides two mean of controlling its thermal conductivity to meet desired specifications in the design on nanotechnology devices. Increasing the channel size increases the thermal conductivity along the planes, while increasing the Cu concentration will decrease the thermal conductivity along the planes, but will increase it across the planes. This combination of thermal control mechanisms allows for multiple ways to reach specific thermal conductivity values, making MoTe$_2$ a versatile material in nanotechnology development.

CHAPTER 5: THERMAL CONDUCTIVITY OF NUCLEAR PASTA

5.1 Introduction

In conjunction with the research of Claudio Dorso from the University of Buenos Aires, the Müller-Plathe method was applied to study the thermal transport properties of nuclear matter present in the crust of neutron stars. Neutron stars are small but dense stars that have a relatively high concentration of neutrons in comparison to other stars. They are often formed out of a star that undergoes supernova due to a core collapse, which occurs when the Fe core becomes so dense that the outer layers of the star are rapidly pulled towards it.[55] Because of the incredibly high temperatures ($> 10^9$ K ≈ 0.1 MeV) found within a neutron star, the protons and neutrons that are normally held together in an atomic nucleus possess too much energy to stay in their nucleic form and instead take on new shapes and structures.[56] Two of the more common nuclear structures have cylindrical and slab-like shapes, leading them to be dubbed nuclear "pasta" because of their resemblance to spaghetti and lasagna.[57] (Watanabe and Sonoda) Much is still unknown about neutron stars,[55] and the motivation for this study is to contribute to ongoing research endeavors to better understand the life and behavior of neutron stars, such as their genesis and thermal evolution.

5.2 Simulation Design

To simulate nuclear pasta, the MD simulations need to be configured to reflect the properties of subatomic particles rather than the atomic particles for which MD was designed. Fortunately, the LAMMPS program provides a Lennard-Jones units system that normalizes all values into unitless quantities, allowing the program to work with the small particle size and high temperatures scales found in neutron stars. In this way, the subatomic particles are treated in the same classical manner as atoms. Although this classical approximation would not befit protons and neutrons bound together in a nucleus, it can be applied in the case of nuclear matter in neutrons stars because they break their nucleic

formations and form larger structures in the similar manner as atoms. Furthermore, because electrons are not bound to these structures, but rather exist in a free-flowing sea around them, quantum contributions to thermal transport can be neglected. For the interparticle potentials of the proton-proton, proton-neutron, and neutron-neutron interactions, a table of separation distance versus potential energy is input into the simulation. Each interaction is divided into 5000 values uniformly spaced from 0.00108 to 5.4 fm, except for the proton-proton interaction, which is spaced from 0.004 to 20.0 fm. A portion of these values is plotted in Fig. 5.1. The lasagna structure was the only form of nuclear matter analyzed, and the initial structure was obtained through Professor Dorso. The simulations used the Müller-Plathe method to calculate the thermal conductivity of the lasagna structures at a timestep of 0.4 and a particle swap rate of once every 1,000 timesteps. The simulations were run for 4,000,000 timesteps. In order to avoid a problem with energy drift, a weak Nosé-Hoover thermostat ($\tau = 1,000$ fs) was applied to the entire simulation structure.
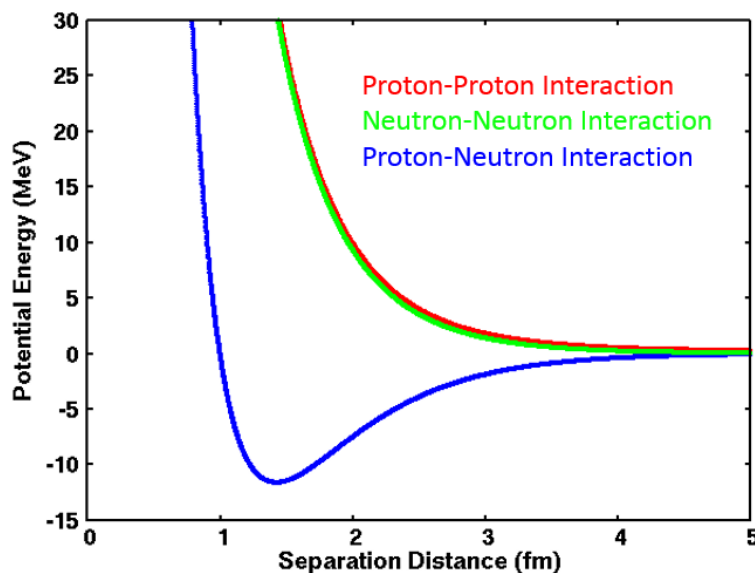
Figure 5.1: Potential energy as a function of separation distance between two protons (red), two neutrons (green), and a proton and a neutron (blue).

5.3 Results and Discussion

Instead of analyzing the size-effects on the thermal conductivity of nuclear lasagna, the goal was to analyze the temperature dependence of thermal conductivity in order to determine how phase changes in the nuclear structure affected its thermal properties. To identify the temperatures at which the lasagna structure undergoes phase changes, a simulation was run in which the lasagna was heated from 0.1 to 2.0 MeV. A graph of energy vs temperature from this simulation is given in Fig. 5.2, along with images depicting the nuclear structure at specific temperatures. Larger images showing the various phases of the lasagna structure are given in Fig. 5.3. These results reveal that the nuclear lasagna first undergoes a transition from crystalline to amorphous near 0.65 MeV (Fig. 5.3a&b), but retains its layered structure until around 0.8 MeV, at which temperature "fingers" begin to form between the layers (Fig. 5.3c). By 1.0 MeV, the layers have completely disappeared into an amorphous, homogenous structure (Fig. 5.3d).
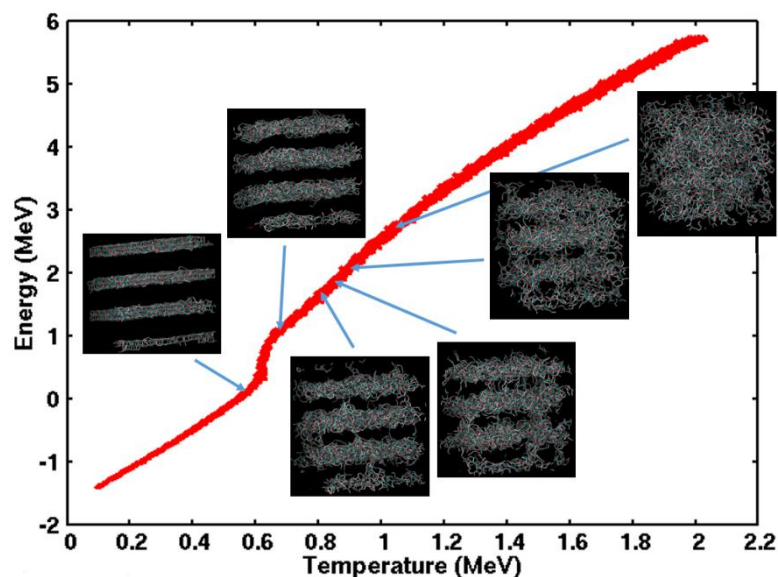
Figure 5.2: Energy vs temperature for the nuclear lasagna structure, demonstrating and depicting the phase transitions of the structure.
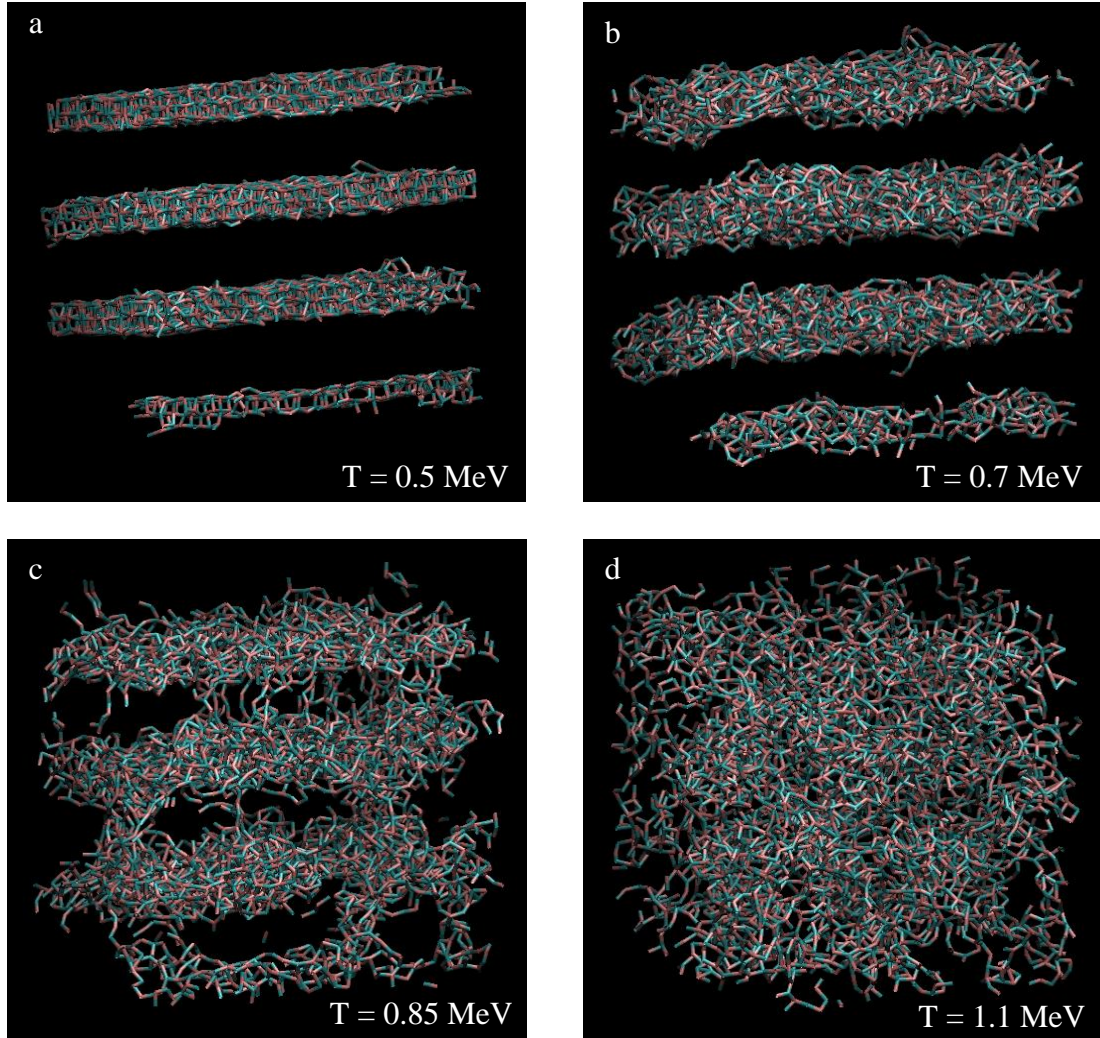
Figure 5.3: Nuclear lasagna structure at temperatures of (a) 0.5 MeV, (b) 0.7 MeV, (c) 0.85 MeV, and (d) 1.1 MeV.

Having established the temperatures at which nuclear pasta undergoes phase transitions, thermal conductivity simulations were run at various temperatures for each phase. At each simulation temperature, two channel lengths were used to gain perspective on the impact of channel length on the simulation results. The results of the simulations are displayed in Fig. 5.4. As temperature increases, the thermal conductivity of nuclear lasagna decreases, which is a common phenomenon since the higher energy vibrations of atoms at increased energy disrupt the correlation of the vibrations that give rise to phonons. Fig. 5.4 shows a jump in thermal conductivity values for temperatures ranging from 0.5 to 0.55 MeV. The reason for this jump is a problem any NEMD thermal conductivity simulation could

have in calculations near a phase transition of a material. Because of the temperature gradient that is formed within the material, the higher energy portions of the material are in a different phase than the lower energy portions. As such, the two portions of the material have different phonon properties, which means that the different portions of the material have different thermal conductivities. This phenomenon can cause a change in the temperature gradient part of the way through the material, which causes difficulties in the thermal conductivity calculations. Consequently, the thermal conductivity values for that portion of the curve have much larger error. The simulation structures that undergo a phase transition part way through are displayed in Fig. 5.5. The bending of the structures occurs because the simulation is kept at constant volume, but the amorphous structure is less dense than the crystalline structure. The bending, therefore, allows the layers to increase in length while retaining the same volume. Factoring this increase in length into the thermal conductivity results leads to only a negligible difference.

Figure 5.4: Thermal conductivity results for nuclear lasagna as a function of temperature. Two channel lengths of 563 fm (green) and 225 fm (red) were used. The thermal conductivity results in the across-layer direction as a function of temperature (blue) are also given.
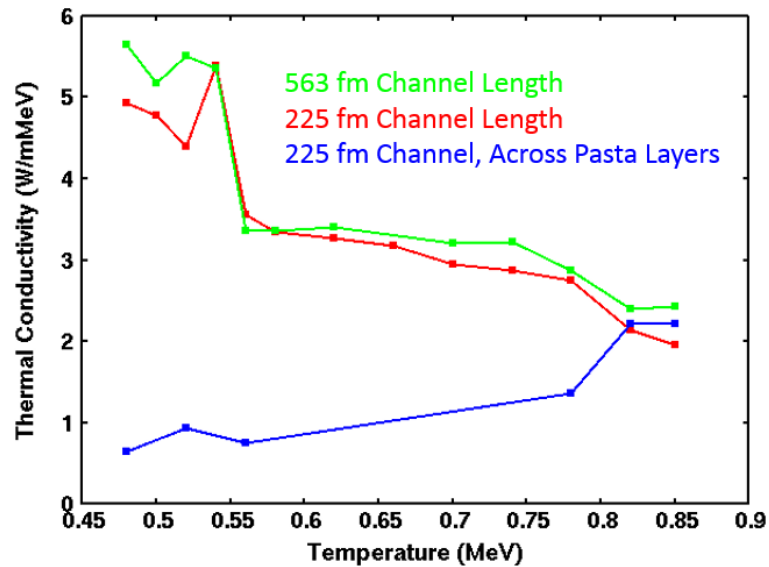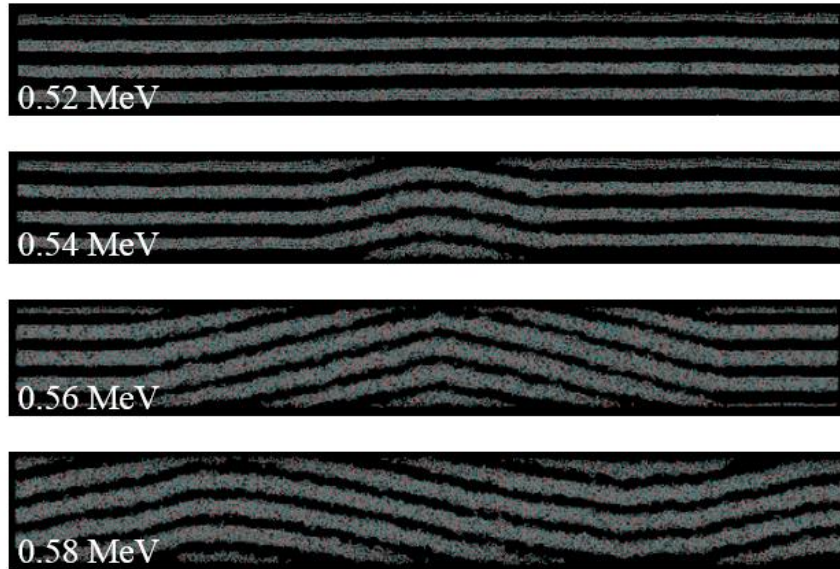
Figure 5.5: Simulation structures for average temperatures of (a) 0.52 MeV, (b) 0.54 MeV, (c) 0.56 MeV, and (d) 0.58 MeV showing the bending that occurs in the portion of the structure that has undergone the crystalline to amorphous transition due to rising in temperature as a part of the Müller-Plathe simulation method.

Also included in Fig. 5.4 are the thermal conductivity values for thermal transport between the lasagna layers. As expected, the thermal conductivities are much lower due to the gaps between the layers eliminating phonon transport between them. As the temperature increases and the layers break apart into a homogenous system, the thermal conductivity in this direction increases to the same values as the calculated in the simulations for thermal conductivity along the lasagna layers.

These thermal conductivity results provide insight into the thermal processes that occur within neutron stars, which can provide additional insight into the behavior of the nuclear matter found inside the star. Ultimately, a better understanding of a star's thermal process will aid in developing a deeper understanding of the lifecycle of a neutron star, including its genesis and thermal evolution. This research also demonstrates the robustness of the MD thermal conductivity simulation methods, in their ability to simulate and analyze atomic and nuclear matters, as well as in conditions much more extreme than those that occur naturally on the earth or even what is obtainable in a laboratory.

CHAPTER 6: CONCLUSION

In this research MD simulations were used to investigate the nanoscale thermal properties of materials that are of interest to the areas of materials science and nuclear physics. In the process, two methods of thermal conductivity calculations using MD were examined to evaluate their abilities to simulate nanoscale thermal transport and to identify their inherent strengths and weaknesses. The examination of the Nosé-Hoover and Langevin thermostats used in the thermostat method led to the conclusion that the nanoscale thermal transport properties of a material can depend on the means of energy input into that material. Using these two thermostats, it was demonstrated that by keeping all other variables fixed and only switching the method of energy input, the thermal conductivity of a Si thin film with a thickness of 150 nm can more than double in magnitude from 80 to 190 W/mK. The reason for the increase in thermal conductivity is the affect the Langevin thermostat has on the phonon modes of the material, whereas the Nosé-Hoover thermostat has no effect on the normal phonon modes. By extrapolating the thermal conductivity values out to bulk dimensions, it was demonstrated that this effect of energy input is only a nanoscale phenomenon. Having also computed thermal conductivity values using the Müller-Plathe method, the evaluation of the three thermal conductivity methods concluded that the Müller-Plathe method and the Nosé-Hoover thermostat method were in close agreement with each other and with published results, while the Langevin method gave greater thermal conductivity values due to its influence of the phonon modes of the system. It must be considered in evaluating these results that, although other published MD results agree with the Nosé-Hoover values, the Stillinger-Weber potential used in these simulations is known to overestimate the experimental thermal conductivity of Si.

As part of evaluating the MD simulation methods using Si, the thermal conductivity of Si thin films and nanowires as a function of size were computed. The results indicate that

thin film thermal conductivity varies greatly with film thickness, covering a range of 10-80 W/mK for thicknesses of 10-150 nm. On the other hand, nanowire thermal conductivity varies little with length, plateauing at a thermal conductivity of 13 W/mK for lengths greater than 80 nm. However, the nanowire thermal conductivity can be increased from 13 W/mK to 28 W/mK by increasing the cross-sectional area from 30 nm^2 to 500 nm^2. Because of the ranges of thermal conductivity values covered by thin films and nanowires with varying thicknesses and cross-sectional areas, the exact thermal conductivity of nanoscale Si can be engineered using its dependence on size to meet precise design specifications in nanoscale devices.

Applying the Müller-Plathe simulation to analyze the thermal properties of $MoTe_2$ broke ground in calculating the thermal conductivity of $MoTe_2$. The results reveal a very low thermal conductivity for $MoTe_2$, on the order of 1-6 W/mK, making it a promising material in thermoelectric applications. These results also demonstrated the variability of the thermal conductivity results with changes in the PDOS of the material. The thermal conductivity simulations of Cu-intercalated $MoTe_2$ revealed a decrease in thermal conductivity along the $MoTe_2$ layers due to the Cu atoms disrupting the normal vibrational patterns of the atoms, but they also demonstrated that intercalated Cu increases the across layer thermal conductivity by connecting the vibrations of multiple layers and allowing phonons to pass between them. In fact, the resulting thermal conductivity was higher in this direction than in any other direction for any concentration of Cu. The ability for Cu to be intercalated into the $MoTe_2$ structure makes it a versatile material in nanotechnology development, since the exact Cu concentration will determined the exact thermal properties of the material.

The Müller-Plathe simulation method was, last of all, applied in analyzing the thermal conductivity of the nuclear matter found in neutron stars. Because nuclear matter undergoes phase transitions within the range of temperature found in neutrons stars, the dependency of thermal conductivity on temperature was examined rather than its dependency on size. The nuclear lasagna structure undergoes two phase transitions within the range of 0.4-1.0 MeV. At around 0.6 MeV, the crystalline lasagna layers become amorphous, and at around 0.8 MeV, the layers break down and form a homogeneous structure. The simulation on each phase resulted in a thermal conductivity of around 5 W/mMeV for the crystalline layers, 3 W/mMeV for the amorphous layers, and 2.3 W/mMeV

for just beyond the breakdown of the layered structure. This research into the thermal properties of neutron stars demonstrates the robustness of MD to be able to simulate both atomic and nuclear matter, as well as its ability to simulate matter in the extreme conditions present in neutron stars.

REFERENCES

REFERENCES

1. E. Pop and K. E. Goodson, "Thermal phenomena in nanoscale transistors," *IEEE* **128**, 102 (2004)

2. R. Mahajan, "Cooling a microprocessor chip," *IEEE* **94**, 1476 (2006)

3. J. Christofferson, K. Maize, Y. Ezzahri, J. Shabani, X. Wang, and A. Shakouri, "Microscale and nanoscale thermal characterization techniques," *J. Electron. Packag* **130**, 041101 (2008)

4. A. D. McConnell and K. E. Goodson, "Thermal conduction in micro- and nanostructures," *Annual Rev. Heat Transfer* **14**, 129 (2005)

5. M. Asheghi, M. N. Touzelbaev, K. E. Goodson, Y. K. Leung, S. S. Wong, "Temperature-dependent thermal conductivity of single-crystal silicon layers in SOI substrates," **120**, 30 (1998)

6. D. G. Cahill, P. V. Braun, G. Chen, D. R. Clarke, S. Fan, K. E. Goodson, P. Keblinski, W. P. King, G. D. Mahan, A. Majumdar, H. J. Maris, S. R. Phillpoit, E. Pop, and L. Shi, "Nanoscale thermal transport. II. 2003-2012," *Appl. Phys. Rev.* **1**, 011305 (2014)

7. D. G. Cahill, K. Goodson, and A. Majumdar, "Thermometry and thermal transport in micro/nanoscale solid-state devices and structures," *J. Heat Transfer* **124**, 223 (2002)

8. A. I. Hochbaum and P. Yang, "Semiconductor nanowires for energy conversion," *Chem. Rev.* **110**, 527 (2009)

9. A. J. Minnich, M. S. Dresselhaus, Z. F. Ren, and G. Chen, "Bulk nanostructured thermoelectric materials: current research and future prospects," *Energy Environ. Sci.* **2**, 466 (2009)

10. A. I. Boukai, Y. Bunimovich, J. Tahir-Kheli, J. Yun, W. A. Goddard III, and J. R. Heath, "Silicon nanowires as efficient thermoelectric materials," *Nature* **451**, 168 (2008)

11. A. Majumdar, "Thermoelectricity in semiconductor nanostructures," *Science* **303**, 777 (2004)

12. M. Hu and D. Poulikakos, "Si/Ge superlattice nanowires with ultralow thermal conductivity," *Nano Lett.* **12**, 5487 (2012)

13. A. I. Hochbaum, R. Chen, R. D. Delgado, W. Liang, E. C. Garnett, M. Najarian, A. Majumdar, and R. Yang, "Enhanced thermoelectric performance of rough silicon nanowires," *Nature* **451**, 163 (2007)

14. D. Dragoman and M. Dragoman, "Giant thermoelectric effect in graphene," *Appl. Phys. Lett.* **91**, 203116 (2007)

15. L. T. Kong, "Phonon dispersion measured directly from molecular dynamics simulations," *Comput. Phys. Comm.* **182**, 2201 (2011)

16. P. K. Schelling, S. R. Phillpot, and P. Keblinski, "Comparison of atomic-level simulation methods for computing thermal conductivity," *Phys. Rev. B* **65**, 144306 (2002)

17. G. Chen, "Phonon heat conduction in nanostructures," *Int. J. Therm. Sci.* **39**, 471 (2000)

18. J. Bodzenta, "Nanoscale heat transport," *Mat. Sci.-Pol.* **26**, 95 (2008)

19. W. Kim, R. Wang, and A. Majumdar, "Nanostructuring expands thermal limits," *Nano Today*, **2**, 40 (2007)

20. C. W. Chang, D. Okawa, H. Garcia, A. Majumdar, and A. Zettl, "Breakdown of Fourier's law in nanotube thermal conductors," *Phys. Rev. Lett.* **101**, 075903 (2008)

21. N. Yang, G. Zhang, and B. Li, "Violation of Fourier's law and anomalous heat diffusion in silicon nanowires," *Nano Today* **5**, 85 (2010)

22. J. Maassen and M. Lundstrom, "Steady-state heat transport: ballistic-to-diffusive with Fourier's law," *J. App. Phys.* **117**, 135102 (2015)

23. P. Chantrenne and J. L. Barrat, "Finite size effects in determination of thermal conductivities: comparing molecular dynamics results with simple models," *J. Heat Trans.* **126**, 577 (2004)

24. S. Nosé, "A unified formulation of the constant temperature molecular dynamics methods," *J. Chem. Phys.* **81**, 511 (1984)

25. W. G. Hoover, "Canonical dynamics: equilibrium phase-space distributions," *Phys. Rev. A* **31**, 1695 (1985)

26. K. Jolly and S. P. A. Gill, "Modelling transient heat conduction in solids at multiple length and time scales: a coupled non-equilibrium molecular dynamics/continuum approach," *J. Comp. Phys.* **228**, 7412 (2009)

27. N. Grønbech-Jensen and O. Farago, "Constant pressure and temperature discrete-time Langevin molecular dynamics," *J. Chem. Phys.* **141**, 194108 (2014)

28. F. Müller-Plathe, "A simple nonequilibrium molecular dynamics method for calculating the thermal conductivity," *J. Chem. Phys.* **106**, 6082 (1997)

29. K. Lin and A. Strachan, "Thermal transport in SiGe superlattice thin films and nanowires: effects of specimen and periodic lengths," *Phys. Rev. B*, **87**, 115302 (2013)

30. J. Q. Broughton and X. P. Li, "Phase diagram of silicon by molecular dynamics," *Phys. Rev. B* **35**, 9120 (1987)

31. S. J. Cook and P. Clancy, "Comparison of semi-empirical potential functions for silicon and germanium," *Phys. Rev. B* **47**, 7686 (1993)

32. M. D. Kluge, J. R. Ray, and A. Rahman, "Molecular dynamic calculation of elastic constants of silicon," *J. Chem. Phys.* **85**, 4028 (1986)

33. J. S. Kallman, W. G. Hoover, C. G. Hoover, A. J. De Groot, S. M. Lee, and F. Wooten, "Molecular dynamics of silicon indentation," *Phys. Rev. B* **47**, 7705 (1993)

34. F. H. Stillinger and T. A. Weber, "Computer simulation of local order in condensed phases of silicon," *Phys. Rev. B* **31**, 5262 (1985)

35. Z. Jian, Z. Kaiming, and X. Xide, "Modification of Stillinger-Weber potentials for Si and Ge," *Phys. Rev. B* **41**, 12915 (1990)

36. R. L. C. Vink, G. T. Barkema, W. F. van der Weg, and N. Mousseau, "Fitting the Stillinger-Weber potential to amorphous silicon," *J. Non-Crys. Solids* **282**, 248 (2001)

37. Z. Zhang and Z. Sun, "Thermal conductivity of silicon thin films predicted by molecular dynamics simulations and theoretical calculation," *App. Mech. Mat.* **55-57**, 1153 (2011)

38. D. P. Sellan, J. E. Turney, A. J. H. McGaughey, and C. H. Amon, "Cross-plane phonon transport in thin films," *J. App. Phys.* **108**, 113524 (2010)

39. C. Jeong, S. Datta, and M. Lundstrom, "Thermal conductivity of bulk and thin-film silicon: A Landauer approach," *J. App. Phys.* **111**, 093708 (2012)

40. S. G. Volz and G. Chen, "Molecular-dynamics simulation of thermal conductivity of silicon crystals," *Phys. Rev. B* **61**, 2651 (2000)

41. X. Yang, A. C. To, and R. Tian, "Anomalous heat conduction behavior in thin finite-size silicon nanowires," *Nanotech.* **21**, 155704 (2010)

42. A. H. C. Neto, F. Guinea, N. M. R. Peres, K. S. Novoselov, and A. K. Geim, "The electronic properties of graphene," *Rev. Mod. Phys.* **82**, 109 (2009)

43. A. K. Geim, "Graphene: status and prospects," *Science* **324**, 1530 (2009)

44. M. Chhowalla, H. S. Shin, G. Eda, L. Li, K. P. Loh, and H. Zhang, "The chemistry of two-dimensional layered transition metal dichalcogenides nanosheets," *Nature Chem.* **5**, 263 (2013)

45. S. Bhattacharyya and A. K. Singh, "Semiconductor-metal transition in semiconducting bilayer sheets of transition-metal dichalcogenides," *Phys. Rev. B* **86**, 075454 (2012)

46. S. Kumar and U. Schwingenschlögl, "Thermoelectric response of bulk and monolayer $MoSe_2$ and WSe_2," *Chem. Mater.* **27**, 1278 (2015)

47. Y. Cai, J. Lan, G. Zhang, and Y. Zhang, "Lattice vibrational modes and phonon thermal conductivity of monolayer MoS_2," *Phys. Rev. B* **89**, 035438 (2014)

48. W. Huang, H. Da, and G. Liang, "Thermoelectric performance of MX_2 (M=Mo,W; X=S,Se) monolayers," *J. App. Phys.* **113**, 104304 (2013)

49. M. Yamamoto, S. T. Wang, M. Ni, Y. Lin, S. Li, S. Aikawa, W. Jian, K. Ueno, K. Wakabayashi, and K. Tsukagoshi, "Strong enhancement of Raman scattering from a bulk-inactive vibrational mode in few-layer $MoTe_2$, *ACS Nano* **8**, 3895 (2014)

50. C. Ataca, H. Şahin, and S. Ciraci, "Stable, single-layer MX_2 transition-metal oxides and dichalcogenides in a honeycomb-like structure," *J. Phys. Chem.* **116**, 8983 (2012)

51. J. N. Coleman, M. Lotya, and A. O'Neill, *et. al*, "Two-dimensional nanosheets produced by liquid exfoliation of layered materials," *Science* **331**, 568 (2011)

52. G. Henkelman, A. Arnaldsson, and H. Jónsson, "A fast and robust algorithm for Bader decomposition of charge density," *Comp. Mat. Sci.* **36**, 354 (2006)

53. T. Böker, R. Severin, A. Müller, C. Janowitz, R. Manzke, D. Vob, P. Krüger, A. Mazur, and J. Pollmann, "Band structure of MoS_2, $MoSe_2$, and α-$MoTe_2$: angle-resolved photoelectron spectroscopy and *ab initio* calculations," *Phys. Rev. B* **64**, 235305 (2001)

54. J. Kim, S. M. Choi, W. Seo, and W. Cho, "Thermal and Electronic properties of Exfoliated Metal Chalcogenides," *Bull. Korean. Chem. Soc.* **31**, 3225 (2010)

55. P. N. Alcain, P. A. Giménez Molinelli, and C. O. Dorso, "Beyond nuclear 'pasta': phase transitions and neutrino opacity of new 'pasta' phases," *Phys. Rev. C* **90**, 065803 (2014)

56. P. A. Giménez Molinelli and C. O. Dorso, "Finite size effects in neutron star and nuclear matter simulations," *Nucl. Phys. A* **933**, 306 (2015)

57. G. Watanabe and H. Sonoda, "Recent progress on understanding 'pasta' phases in dense stars," *AIP Conf. Proc.* **791**, 101 (2005)